Chapter 3

Radiative effects of supercooled water layers

Summary. Supercooled liquid water layers are visible in lidar imagery as a strongly enhanced return followed by rapid extinction of the beam, suggesting that they are radiatively important. In this chapter, three profiles of liquid and ice extinction coefficient, water content and effective radius are retrieved from the remote measurements made during the ESA-funded 1998 Cloud Lidar And Radar Experiment. Radar-lidar and dual-wavelength radar techniques were used to size the ice particles and where *in situ* validation was available, agreement was good. Radiative transfer calculations were then performed on these profiles to ascertain the radiative effect of the supercooled water[1]. It was found that, despite their low liquid water path (generally less than 10–20 g m^{-2}), these clouds caused a significant increase in the reflection of solar radiation to space, even when cirrus was present above which dominated the long-wave signal. In the cases considered, their capacity to decrease the net absorbed radiation was at least twice as large as that of the ice. The layers were typically 100–200 m thick, suggesting that they are unlikely to be adequately represented by the resolutions of current forecast and climate models. These results suggest that a spaceborne lidar and radar would be ideally suited to characterizing the occurrence and climatological importance of mixed-phase clouds on a global scale.

3.1 Introduction

Mixed-phase clouds have the potential to play an important role in the climate system (Li and Le Treut 1992; Sun and Shine 1995; Gregory and Morris 1996), but this is difficult to quantify due to a lack of good observational datasets and knowledge of their microphysical parameters. Hence cloud phase parameterizations in numerical forecast and climate models have tended to remain rather crude, involving typically a single prognostic variable for cloud water content that is divided into liquid and ice on the basis of temperature alone. Some recent, more physically based parameterizations use other model variables (such as vertical velocity) to aid the diagnosis of liquid/ice fraction (Tremblay *et al.* 1996), while others go further and use separate prognostic variables for ice and liquid water (Wilson and Ballard 1999). Clearly long-term observations from the ground and from space are needed, both for direct evaluation of model forecasts, and to build up a climatology against which climate models may be tested.

Previously in ESA reports (ESA 1999a, Illingworth et al. 2000), data from the 1998 Cloud Lidar And Radar Experiment (CLARE'98) has been used to demonstrate that the combination of radar and lidar offers a straightforward way to infer the presence of supercooled liquid water in stratiform clouds.

[1]The calculations were performed by Peter Francis of the UK Met Office, as part of Hogan *et al.* (2003) paper.

Because of the vastly larger concentration of cloud condensation nuclei than ice nuclei in the atmosphere, when supercooled water clouds are formed the available liquid water is distributed amongst a large number of small droplets, while ice particles are typically larger and much less numerous. Since at lidar wavelengths cloud particles scatter in the geometric optics regime, the backscattered intensity is approximately proportional to the square of particle diameter, and so large numbers of small liquid water droplets can easily dominate the signal when they are present. Conversely, the radar operates in or close to the Rayleigh scattering regime, and the echo power is approximately proportional to the square of particle mass. Thus radar reflectivity factor (Z) is always dominated by the larger ice particles, even when liquid water is present. Supercooled liquid water tends to be strikingly visible to the lidar as thin but highly reflective layers.

In this chapter a one-dimensional radiation model is used to estimate the radiative effect of the supercooled liquid water layers observed in CLARE'98, using realistic profiles of liquid and ice water content and effective radius retrieved from the remote measurements made in the two case studies. A crucial aspect to this is using airborne lidar data in order to get an unobscured view of the liquid water layers, particularly the uppermost layer in the case of multiple layers as this is crucial to determining the top-of-atmosphere fluxes. We use both the radar-lidar backscatter ratio and the ratio of radar reflectivities measured at 35 and 94 GHz to estimate ice particle size, techniques which have also been proposed for use from space (ESA 1999b; Hogan and Illingworth 1999). In section 3.2 the instruments used are described, and in section 3.3.1 it is shown how three mixed-phase profiles are retrieved from them, with some in situ validation. Then in section 3.4 the relative radiative importance of ice and liquid water in each profile is evaluated. The results in this chapter have been published (Hogan et al. 2003).

3.2 Measurements during CLARE'98

The CLARE'98 campaign took place at Chilbolton, England, between 5 and 23 October 1998, funded by the European Space Agency to support the development of retrieval algorithms for a future spaceborne cloud radar and lidar. Details of the many ground-based and airborne instruments that were involved may be found in ESA (1999a). The profiles used are from two of the seven flights, on 20 and 21 October 1998. The three aircraft flew coordinated runs towards and away from Chilbolton along the 260° azimuth. The DLR (German Centre for Aeronautics and Space-flight) *Falcon* aircraft flew at an altitude of around 13 km and observed the cloud from above with its nadir-viewing polarimetric 'ALEX' lidar. Meanwhile the French ARAT (Aircraft for Atmospheric Research and Remote Sensing) flew at an altitude of around 5 km and observed the clouds with its polarimetric *Leandre* lidar. The UK Met Office C-130 aircraft then made *in situ* measurements of the cloud with its comprehensive array of microphysical probes. The inbound overhead times of the aircraft were synchronized, and at the end of each inbound run and start of each outbound run the clouds were also observed by three vertically pointing cloud radars and a 905-nm Vaisala CT75K lidar ceilometer (used extensively in the next chapter) on the ground at Chilbolton. These instruments are now described in more detail.

3.2.1 Airborne lidar observations

The ALEX lidar on board the *Falcon* aircraft makes use of an Nd:YAG laser to provide measurements of attenuated backscatter coefficient (β') at 1064, 532 and 355 nm. In addition to the cloud return, the shorter wavelengths are able to detect molecular scattering, thus providing a means of absolute calibration as well as the possibility of measuring optical depth using the molecular return from the far side of the cloud. This can then be used to correct the measured β' values for attenuation, provided of course that the molecular echo is not so attenuated that it cannot be detected. A depolarization channel is also available at 532 nm, providing information on the phase of the target hydrometeors. The performance of the system was described fully by Mörl *et al.* (1981). The specification of the *Leandre* lidar on the ARAT aircraft is rather similar to that of ALEX, and is described by Pelon *et al.* (1990). It can be pointed either at nadir or zenith.

3.2.2 Ground-based radar observations

Three ground-based cloud radars were used in combination with the airborne lidars to retrieve profiles of cloud properties for input into a one-dimensional radiation model (see section 3.4). The permanent Chilbolton 94-GHz *Galileo* radar and the transportable 95-GHz *Miracle* radar of the GKSS Institute for Atmospheric Physics in Germany (Quante *et al.* 1998) were both operated continuously at zenith. The 35-GHz *Rabelais* radar, on loan from the University of Toulouse, was mounted on the side of the main 25-m dish to permit scanning with CAMRa, which meant that it was not always at vertical at the times of the aircraft overflights of Chilbolton. During the overflights the *Miracle* radar switched to an operational mode that permitted recording of the full Doppler spectrum of particle fall velocities, but which limited the sampling window to a 2.5-km range enclosing the height of the C-130.

The cloud radars were calibrated by comparison with the 3-GHz Chilbolton weather radar; firstly the 3-GHz and 35-GHz radars were matched up while scanning through light, Rayleigh-scattering rain, and then the *Galileo* and *Miracle* were compared with the *Rabelais* while dwelling vertically in thin low-level liquid water cloud (for details see Hogan and Goddard 1999). Correction for attenuation by atmospheric gases was performed using the line-by-line model of Liebe (1985) together with temperature and humidity profiles from the mesoscale version of the Met Office Unified Model. Liquid water attenuation can also be a problem at 94 GHz, but the profiles analysed in section 3.4 were from occasions with no low cloud present. The liquid water path of the supercooled clouds was generally less than 10 g m^{-2} (see section 3.4), which at $-15°$C would cause a two-way 94-GHz attenuation of only around 0.08 dB, so can be neglected. Ice attenuation is negligible at these frequencies (Hogan and Illingworth 1999).

3.2.3 The UK Met Office C-130 aircraft

The Met Office C-130 Hercules carried a comprehensive array of microphysical probes suitable for characterizing mixed-phase clouds. Bulk ice water content (IWC) was estimated by integrating size spectra derived from two imaging probes: the 2D cloud (2D-C) and 2D precipitation (2D-P) probes measured hydrometeors in the diameter ranges 25–800 μm and 200–6400 μm respectively, and are based on the instrument described by Knollenberg (1970). The mass-area relationship of Francis *et al.* (1998) was used in order to minimize the differences with IWC derived using the evaporative technique of Brown (1993). Bulk liquid water content (LWC) was provided by a Johnson-Williams hot-wire probe. The Forward Scattering Spectrometer Probe (FSSP) counts particles in the diameter range 2–47 μm, although because over-counting may occur when large ice particles are present (Gardiner and Hallett 1985) we use only the effective droplet radius reported by this instrument. The distribution is truncated at a diameter of 30 μm to minimize ice contamination, although this generally changes effective radius by less than 10%.

3.3 Retrieval of mixed-phase cloud profiles

Three profiles of extinction coefficient and effective radius are retrieved from the remote observations, which in the next section are used as input to a radiative transfer model. Profiles of ice cloud properties are obtained by combining backscatter measurements at two different frequencies and utilizing the different size dependence of the backscattering efficiency to derive particle size. The radar/lidar method was first used by Intrieri *et al.* (1993) and has the potential to be accurate because of the much stronger dependence of radar reflectivity factor on size compared with lidar backscatter coefficient. However, correction must first be made for attenuation of the lidar signal. When lidar attenuation is too strong, such as in the presence of supercooled liquid water clouds, we make use of 35-GHz and 94-GHz radars; the larger ice particles scatter outside the Rayleigh regime at the higher frequency and the ratio of reflectivity at the two wavelengths can be related to particle size (Sekelsky *et al.* 1999; Hogan *et al.* 2000). The retrieval of the liquid properties is described separately for each of the three profiles.

It should be noted that the principal objective in this section is to get an idea of the typical radiative effect that supercooled liquid water could have in realistic mixed-phase clouds, not to rigorously evaluate the lidar-radar and dual-wavelength radar methods for retrieving ice particle properties. Hence moderate errors in the retrievals are tolerable for these purposes.

3.3.1 Retrieval of ice properties

We assume that the ice particle size distribution $n(D)$ may be described by a gamma distribution:

$$n(D) = N_0 D^{\mu} \exp\left(-\left[3.67+\mu\right] D/D_0\right), \tag{3.1}$$

where D is the equivalent-area diameter (i.e. the diameter of a sphere with the same cross-sectional area as the actual particle), D_0 is the median volume diameter, and μ is the 'shape parameter' of the distribution. N_0 is a concentration scaling parameter and is eliminated when the ratio of backscatter at two different frequencies is calculated.

Ice particles are assumed to scatter according to geometric optics at lidar wavelengths, with the result that the visible extinction coefficient, α, is proportional to twice the cross-sectional area:

$$\alpha = \frac{\pi}{2}\int_0^{\infty} n(D) D^2 \, dD, \tag{3.2}$$

while at radar frequency f we assume that the ice particles may be approximated as homogeneous spheres with the same mass and cross-sectional area, and radar reflectivity is then given by:

$$Z_f = |K_{\mathrm{i}}|^2 \int_0^{\infty} n(D) \left(\frac{\rho}{\rho_{\mathrm{i}}}\right)^2 D^6 \gamma_f(D)\, dD, \tag{3.3}$$

where $|K_{\mathrm{i}}|^2$ is the 'dielectric factor' of solid ice (essentially constant at 0.174 for frequencies between 0.1 and 1000 GHz), $\gamma_f(D)$ is the Mie/Rayleigh backscattering ratio, ρ is the effective density of the ice-air mixture and ρ_{i} is the density of solid ice. We have applied Debye's solution (Battan 1973), in which radar reflectivity is proportional to the square of the effective density. Francis *et al.* (1998) derived the following relationship between mass m and cross-sectional area A from a large aircraft dataset (although they expressed their relationship in terms of melted-equivalent diameter):

$$\begin{aligned} m &= 0.691 A^{1.5}\ \mathrm{mg}; \quad A \leq 0.0052\ \mathrm{mm}^2 \\ m &= 0.122 A^{1.17}\ \mathrm{mg}; \quad A > 0.0052\ \mathrm{mm}^2, \end{aligned} \tag{3.4}$$

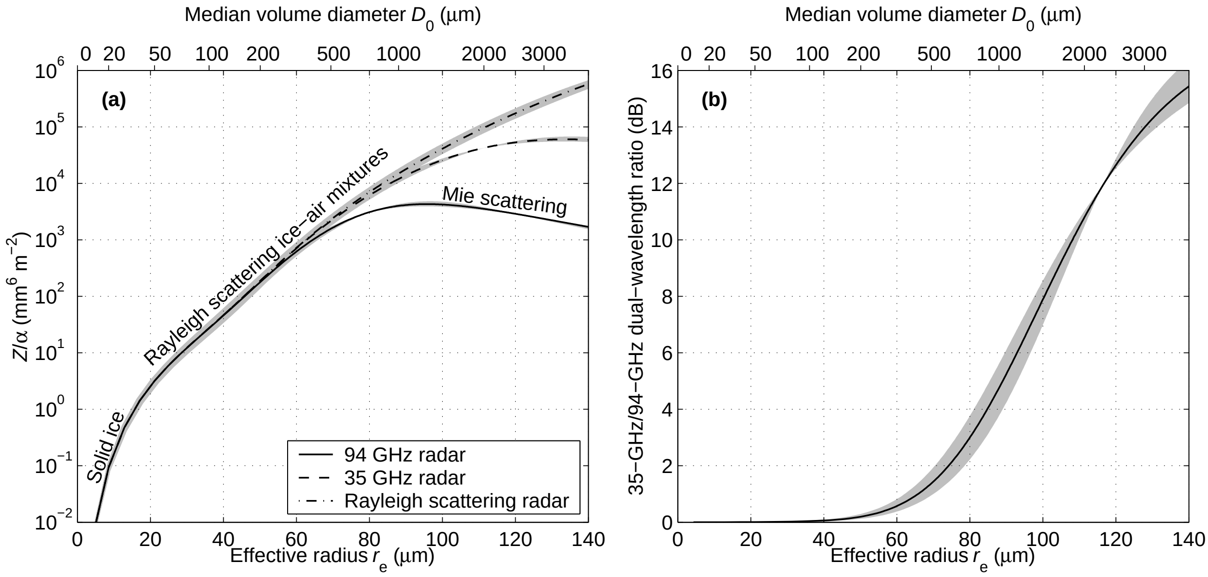

Figure 3.1: Variation of (a) radar-lidar ratio and (b) dual-wavelength radar ratio, with effective radius. The black lines indicate the results for shape parameter μ of 1 in (3.1), while the grey bands indicates the range of retrievals associated with μ varying between 0 and 3.

with A measured in mm^2. From this the following expression for density as a function of equivalent-area diameter (in mm) may be derived (Hogan *et al.* 2000):

$$\begin{aligned} \rho &= 0.917 \text{ g m}^{-3}; & D &\leq 0.081 \text{ mm} \\ \rho &= 0.175 D^{-0.66} \text{ g m}^{-3}; & D &> 0.081 \text{ mm}. \end{aligned} \tag{3.5}$$

The impact of uncertainties in density on the retrievals is discussed below. It should be noted that the use of integrals from 0 to infinity in (3.2) and (3.3) is not expected to introduce significant error, since for a first-order gamma distribution with a median volume diameter of 1 mm, 90% of the extinction is attributable to particles of diameter less than 1.4 mm and 90% of the radar reflectivity factor (in the Rayleigh scattering approximation) is attributable to particles smaller than 2.5 mm.

Effective radius was defined for ice clouds by Foot (1988) as

$$r_e = \frac{3}{2}\frac{\text{IWC}}{\rho_i \alpha}, \tag{3.6}$$

and similarly for liquid water clouds. Thus, by considering size distributions with a range of values for D_0, we can simulate the relationship between r_e, radar-lidar ratio and dual-wavelength radar ratio. The results are depicted in Fig. 3.1, for an assumed shape parameter μ of 1. For r_e up to around 60 μm, the radar-lidar method is potentially the most sensitive, with a 20 μm change in r_e corresponding to at least an order of magnitude change in the radar-lidar ratio. However, when $r_e > 80$ μm (which is equivalent to $D_0 > 800$ μm), then Mie scattering acts to reduce the measured radar reflectivity factor at 94 GHz such that it has a similar size dependence to the lidar, with the result that the radar-lidar ratio is almost constant and no size information can be inferred. The same problem occurs at 35 GHz when $r_e > 120$ μm. For $r_e > 60$ μm, however, the ratio of reflectivities at 35 GHz and 94 GHz contains useful size information and has the advantage that it can be used when liquid water is present that would strongly attenuate the lidar signal. The gray bands in Fig. 3.1 indicate the effect of using μ values ranging between 0 and 3; in can be seen that this changes retrieved r_e from the $\mu = 1$ line by only 2.5 μm in the case of the radar-lidar technique and at most 4 μm for the dual-wavelength radar technique. Kosarev and Mazin (1989) found typical values of μ between 0 and 1, although their dimension was based on the maximum physical extent of the particle, rather than the equivalent-area diameter.

Hogan *et al.* (2000) showed that although the dual-wavelength radar technique is fairly insensitive to μ, axial ratio and ice density can potentially be quite important. In the case of axial ratio, we use 3-GHz Z_{DR} to indicate where the assumption of sphericity is significantly in error, and apply the technique only in regions where Z_{DR} is close to 0 dB. Density would therefore seem to be the main uncertainty in the retrieval. Hogan *et al.* (2000) found that the effect on dual-wavelength radar retrievals of using the $\rho = 0.07D^{-1.1}$ g m^{-3} relationship of Brown and Francis (1995) instead of the form shown in (3.5) was a 20% change in the retrieved D_0 and a factor-of-two change in retrieved IWC. It is likely that similar uncertainties are present for IWC and size retrieved using the radar-lidar technique.

3.3.2 Profile 1

The first profile was taken on 20 October 1998 and is shown in Fig. 3.2. The *Falcon* aircraft passed over Chilbolton at 1421 UTC, and the corresponding unattenuated α profile is shown by the thin line in Fig. 3.2a. Attenuation correction was performed using the 355-nm and 532-nm molecular returns at the far side of the cloud to provide a total optical depth constraint, which was then partitioned with height assuming a constant extinction-to-backscatter ratio, or 'lidar ratio' (Klett 1985). The value for the lidar ratio was found to be 15 sr, close to the theoretical value for liquid water droplets. Using lidar ratios of 14 and 17 sr in the inversion changes the retrieved total optical depth by -22% and $+36$% respectively.

Four highly reflective layers, which we assume to be liquid water, were present between 3.8 km and 5.6 km, while cirrus was observed between 9 km and 13 km. The r_{e} of the cirrus was first estimated by combining the lidar α measurements with the reflectivity factor of the 94-GHz *Miracle* (the thick solid line above 9 km in Fig. 3.2a); the result is shown by the thick line in Fig 3.2b, ranging from 20 to 45 μm. The radar did not detect the full extent of the cloud so, for the purposes of the radiation calculations in the next section, we arbitrarily assume a cloud-top r_{e} of 10 μm which increases linearly down to the first radar measurement. At the base of the cirrus, r_{e} is assumed to be constant in the 220 m where the lidar detected the cloud and the radar did not.

The ice properties of the mid-level cloud were estimated by dual-wavelength radar at the time the *Falcon* aircraft passed overhead. Lidar was not used for this purpose because of possible errors due to uncertain attenuation by the liquid water layers, and the fact that small amounts of liquid water could still be present between the layers. The thick solid and dashed lines below 6 km in Fig. 3.2a show the 94-GHz *Galileo* and 35-GHz *Rabelais* radar measurements, respectively. Below 4.5 km the dual-wavelength ratio was large enough to estimate effective radius using the relationship plotted in Fig. 3.1b, and the results are shown in Fig. 3.2b, ranging from 85 to 110 μm. We assume that the ice effective radius at the top of the mid-level cloud is 70 μm, similar to the value obtained at this altitude from radar and lidar in the next profile (Fig. 3.3b). Then from Z and r_{e}, the ice extinction coefficient α was calculated using the relationship plotted in Fig. 3.1b. Ice water content was calculated from r_{e} and α using (3.6). Finally, the peaks in extinction coefficient measured by the ALEX lidar in the mid-level cloud were assumed to be entirely attributable to liquid water, and liquid water content was calculated by assuming that the liquid water effective radius was 4.5 μm for all supercooled liquid water clouds. This was a typical value measured by the C-130 FSSP in the thicker supercooled liquid water clouds on 20 October 1998.

Figures 3.2c and 3.2d show the resulting ice and liquid extinction coefficients and water contents that are to be used in the radiation calculations. Figure 3.2b also shows the corresponding cumulative visible optical depth of the clouds with and without the contribution from liquid water. The optical depth

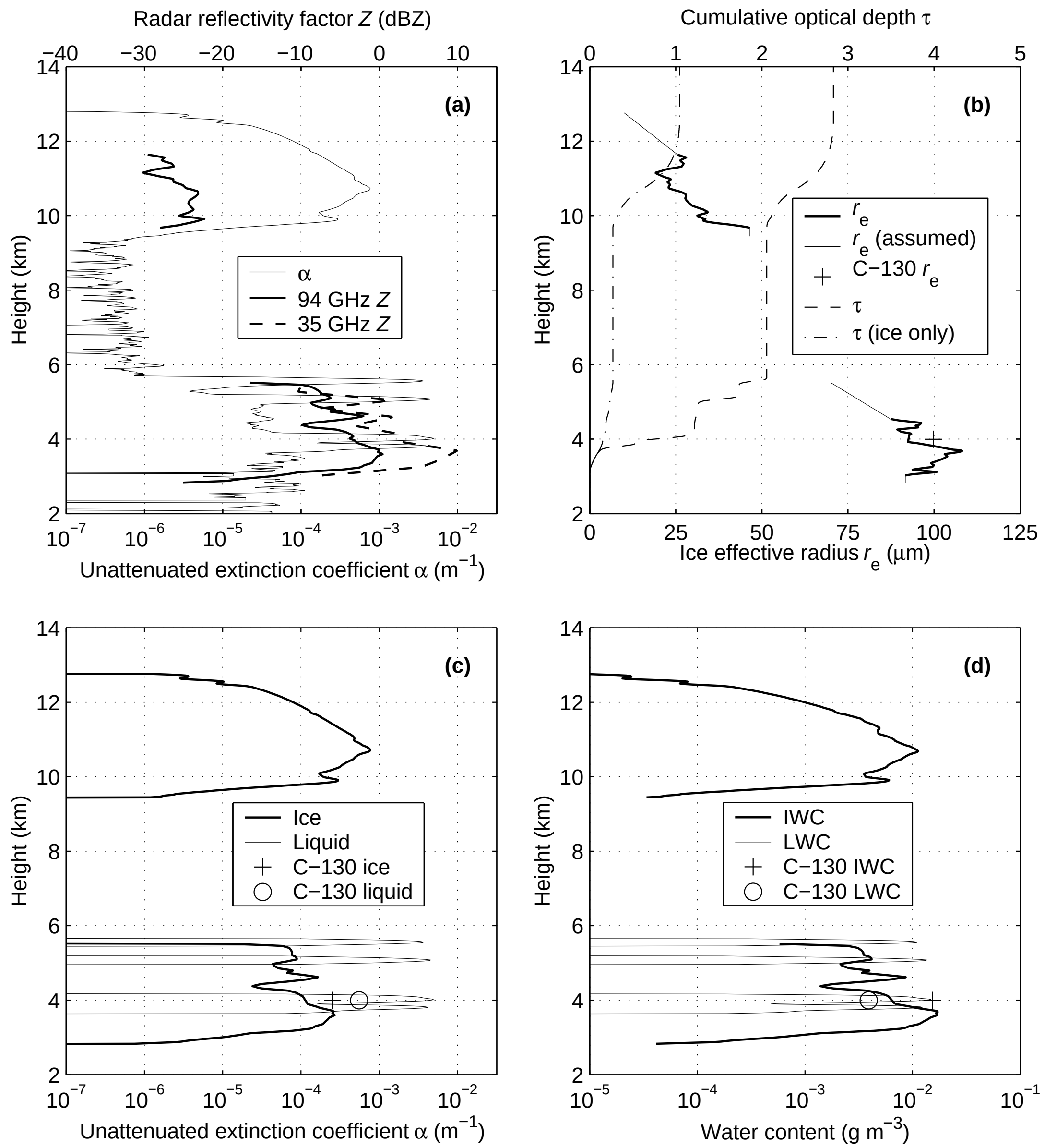

Figure 3.2: Retrieval of ice and liquid cloud properties from lidar and dual-wavelength radar for 'Profile 1', at around 1420 UTC on 20 October 1998: (a) attenuation-corrected extinction profiles from the ALEX lidar and effective radar reflectivity factor from the 35-GHz and 94-GHz radars; (b) ice effective radius derived from the radar and lidar profiles, and cumulative visible optical depth of the ice cloud only and of all cloud; (c) extinction coefficient of the ice and liquid water phases; (d) liquid and ice water content, assuming a liquid effective radius of 4.5 μm. The retrieval process is described fully in the text.

of the mid-level cloud was around 2, although only around 0.25 of this was due to ice. The C-130 aircraft measurements taken as it flew over Chilbolton 1 min earlier at an altitude of 4 km are also plotted in panels b–d. The C-130 measurements of IWC and ice extinction coefficient are around a factor of two larger than those inferred from radar, although r_e is only around 10% larger. At this altitude the C-130 appears to have been flying between the lower two layers, and the liquid water measurements are consistent with those estimated from the lidar.

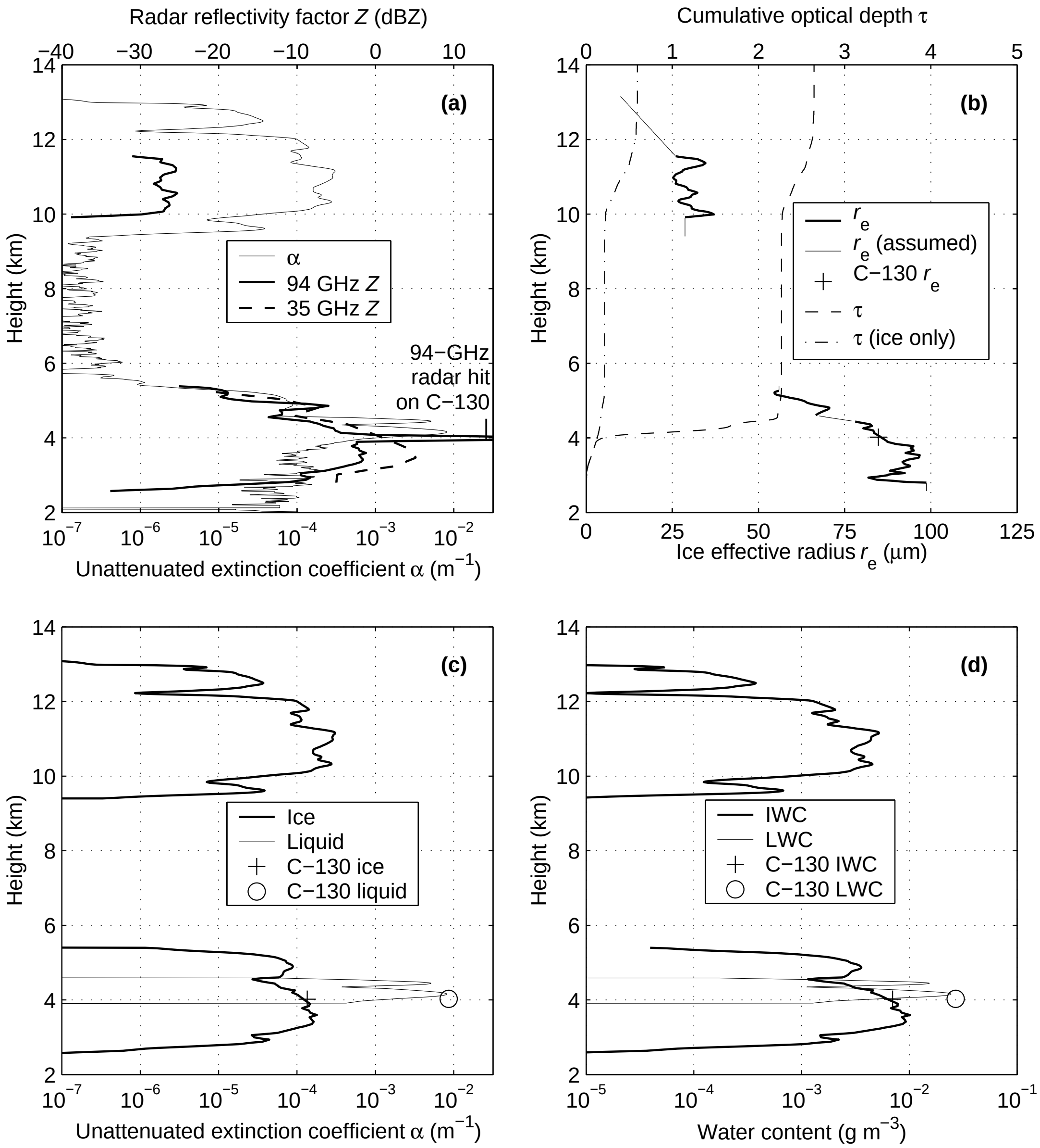

Figure 3.3: Retrieval of ice and liquid cloud properties from lidar and dual-wavelength radar for 'Profile 2', at around 1430 UTC on 20 October 1998. The panels are the same as in Fig. 3.2.

3.3.3 Profile 2

The second profile occurred 12 minutes after the first, when the *Falcon* commenced its outbound leg, and a similar approach was used to calculate the microphysical properties. By this time the visible optical depth of the cirrus had fallen from 0.8 to 0.3, while the liquid water in the mid-level cloud was now concentrated in a double-peaked layer between 4 and 4.5 km that had an optical depth of around 2. Figure 3.3 shows the information for the profile plotted as in Fig. 3.2. The *Miracle* radar was again used in the high cirrus. The nearest vertically pointing 35-GHz data was taken 9 mins earlier (at 1424 UTC) when the C-130 passed overhead at the start of its outbound run and the 35-GHz *Rabelais* started scanning. Since the dual-wavelength radar method can be sensitive to differences in reflectivity due to mismatched beams, the 94-GHz profile nearest to the 35-GHz profile was chosen for retrievals in the mid-level cloud, and was from the *Galileo* radar. The C-130 was 'hit' by the *Galileo* in this profile,

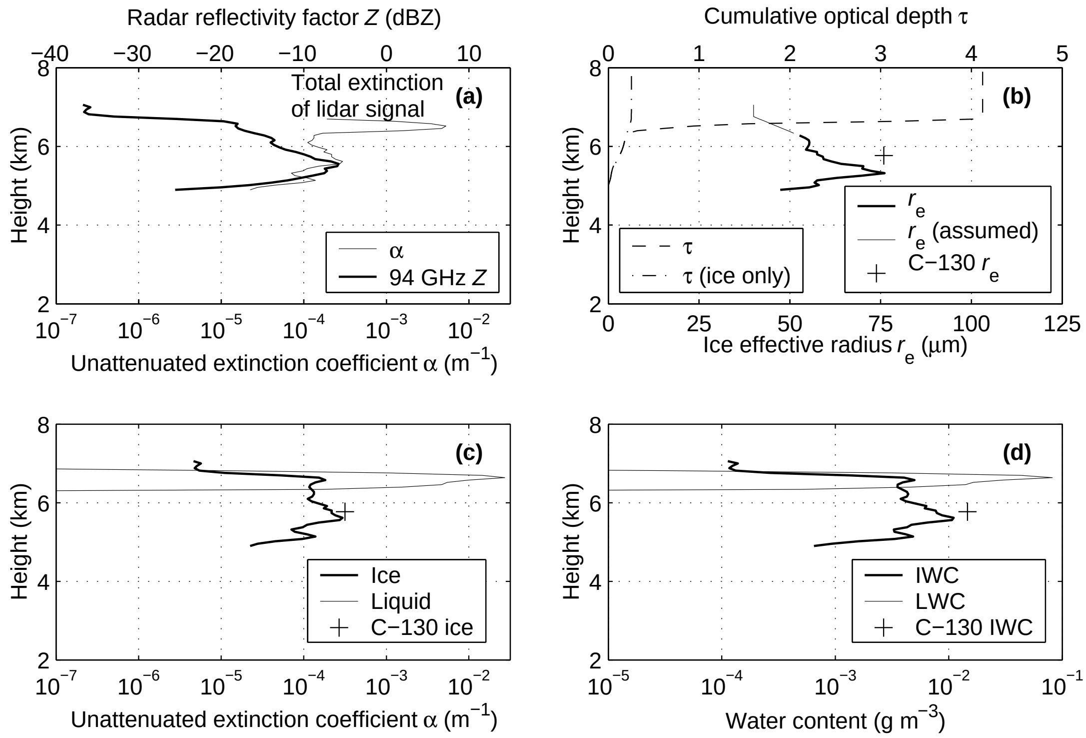

Figure 3.4: Retrieval of ice and liquid cloud properties from lidar and radar for 'Profile 3', at around 1020 UTC on 21 October 1998: (a) attenuation-corrected extinction profiles from the *Leandre* lidar and effective radar reflectivity factor from the 95-GHz *Miracle* radar; (b) ice effective radius derived from the radar and lidar profiles, and cumulative visible optical depth of the ice cloud only and of all cloud; (c) extinction coefficient of the ice and liquid water phases; (d) liquid and ice water content, assuming a liquid effective radius of 4.5 μm.

giving us confidence that *in situ* evaluation of the dual-wavelength retrieval can be performed at exactly the right location. Quante *et al.* (2000) also examined this event and compared the ALEX and *Miracle* profiles in the mid-level cloud at around 1433 UTC.

Above the liquid water layer embedded in the mid-level cloud we use the lidar and 35-GHz radar data to estimate r_e and find it to range from 55 to 70 μm. Below the liquid water layer the dual-wavelength radar ratio indicates r_e ranging from 80 to 100 μm. The C-130 ice measurements at the instant of the overhead are all in excellent agreement with the values inferred from radar (we have interpolated across the strong peak in the *Galileo* signal corresponding to a hit on the aircraft). The C-130 liquid water measurements were taken 8.3 km from Chilbolton, which assuming a radial wind speed of 18 m s^{-1} (taken from the Unified Model) and no cloud evolution, should correspond to the lidar measurements at 1433 UTC. The aircraft measurements of liquid extinction coefficient and water content also agree well with the peak values inferred from lidar.

3.3.4 Profile 3

The final profile was taken from the flight on 21 October 1998. The *Miracle* radar profile at 1028 UTC is shown in Fig. 3.4a, just after it switched from measuring Doppler spectra to its ordinary recording mode. The ALEX lidar receiver saturated in this run, so we use data from the *Leandre* lidar. The ARAT commenced its outbound run 4 mins earlier, so we have assumed a wind speed along the aircraft radial of

Profile	Liquid water path (g m^{-2})	Ice water path (g m^{-2})	Liquid optical depth	Ice optical depth	Optical depth of ice above supercooled water
1	5.4	27.2	1.79	1.04	0.78
2	6.2	17.5	2.05	0.59	0.38
3	11.6	8.9	3.87	0.26	0.00

Table 3.1: Water paths and visible optical depths of the liquid and ice phases, for each of the three profiles discussed in the text.

27 m s^{-1} (from the Unified Model) and found the *Leandre* profile that would have passed over Chilbolton at the time the *Miracle* profile was taken; this is also shown in Fig. 3.4a. An extinction-to-backscatter ratio in ice of 35 sr has been assumed in order to make the slight correction for ice attenuation; the total optical depth of the ice was only around 0.25 (the value of 15 sr found for the profile in Fig. 3.2 was mostly due to liquid water). Below 6.2 km the lidar echo is assumed to be predominantly from ice, and r_e derived from the radar and lidar is shown by the thick line in Fig. 3.4b. The highly reflective liquid water layer above 6.2 km dominated the lidar signal so here we have arbitrarily assumed that the ice r_e dropped linearly to 40 μm at the top of the layer. The C-130 *in situ* ice measurements are also depicted in Fig. 3.4 and show the values derived from radar and lidar to be somewhat underestimated; r_e is 20% lower, α is 30% lower and IWC is around a factor of two too low.

The liquid water layer above 6.2 km completely extinguished the lidar signal, making it impossible to estimate optical depth from the molecular return above the cloud. However, Francis *et al.* (1999) were able to estimate the optical depth of this layer using the passive radiation measurements on board the *Falcon* aircraft; the albedo of 0.45 implied an optical depth of around 4. The extinction coefficient of the liquid water, shown in Fig. 3.4c, has been increased to satisfy this finding.

3.4 Determination of the radiative effect of layers of supercooled water

Radiative transfer calculations using the Edwards and Slingo (1996) scheme have been performed on the three profiles to determine the radiative effect of the supercooled water. The long-wave calculations employed 300 spectral bands, with 220 bands being used in the short-wave. A two-stream delta-Eddington solver was used for the calculations, requiring as input the extinction optical depth, single-scattering albedo $\tilde{\omega}_0$ and asymmetry parameter g for both water and ice clouds. These optical properties were calculated for the water clouds in terms of LWC and r_e using parameterizations of the form presented by Slingo and Schrecker (1982) in both the short-wave and the long-wave. The Mie calculations required to perform these parameterization fits were re-done at a much higher spectral resolution than used in the original Slingo and Schrecker (1982) chapter, in order to utilize the relatively large number of bands used in these comparisons. Hu and Stamnes (1993) have shown that the parameterization of water cloud optical properties in terms of LWC and r_e in this manner yield extremely accurate results when compared with exact calculations.

The ice cloud optical properties were calculated using the parameterization of Fu and Liou (1993), which assumes that the ice crystals are hexagonal columns. Although this crystal shape is probably not the most realistic when compared with the shapes observed in the *in situ* data, especially for the mid-level ice cloud (see Figs. 6 and 11), we have used this parameterization because it does treat the ice cloud optical properties in a consistent manner across both the short-wave and long-wave spectral regions. In order to assess the likely errors associated with selecting an inappropriate crystal shape, we also carried

Profile		albedo	Outgoing long-wave radiation (W m^{-2})	Reflected short-wave radiation (W m^{-2})	Net absorbed radiation (W m^{-2})
1	Clear sky	0.13	245.0	61.5	175.8
	Ice only	0.30	179.4	145.4	157.6
	Liquid only	0.35	219.8	170.2	92.3
	All cloud	0.42	169.2	201.0	112.1
2	Clear sky	0.13	244.8	59.5	154.8
	Ice only	0.25	204.7	112.5	142.0
	Liquid only	0.37	221.3	171.4	66.4
	All cloud	0.41	190.8	186.9	81.5
3	Clear sky	0.12	251.4	70.2	262.5
	Ice only	0.16	240.5	91.2	252.5
	Liquid only	0.45	195.3	260.2	128.6
	All cloud	0.45	194.2	264.4	125.6

Table 3.2: Top-of-atmosphere radiation parameters for each of the three profiles discussed in the text.

Profile		Outgoing long-wave radiation (W m^{-2})	Reflected short-wave radiation (W m^{-2})	Net absorbed radiation (W m^{-2})
1	Effect of ice	−65.7	+83.9	−18.2
	Effect of liquid water	−25.2	+108.7	−83.5
	Effect of ice and liquid water	−75.8	+139.5	−63.7
2	Effect of ice	−40.2	+52.5	−12.8
	Effect of liquid water	−23.5	+111.8	−88.4
	Effect of ice and liquid water	−54.0	+127.4	−73.3
3	Effect of ice	−11.0	+21.0	−10.0
	Effect of liquid water	−56.1	+190.0	−133.9
	Effect of ice and liquid water	−57.3	+194.1	−136.9

Table 3.3: Effects on top-of-atmosphere radiation parameters of ice cloud only, liquid water cloud only, and both ice and liquid water clouds.

out a parallel series of short-wave radiative transfer calculations where either hexagonal plates, bullet-rosettes or planar polycrystals were assumed for the ice crystal optical properties. These single-scattering calculations were carried out using the ray-tracing model described by Macke *et al.* (1996), and the results parameterized as functions of IWC and r_e in a similar manner to that described above. These parallel calculations showed that, when IWC, r_e and (most importantly) optical depth are constrained by the radar/lidar observations, the resulting short-wave fluxes differ by less than 10 W m^{-2}. The effects of changing crystal shape in the long-wave will be even smaller than in the short-wave, because ice absorption is so strong over much of the relevant thermal infrared region. These arguments suggest that the choice of crystal shape will not significantly affect any of our subsequent conclusions on the relative

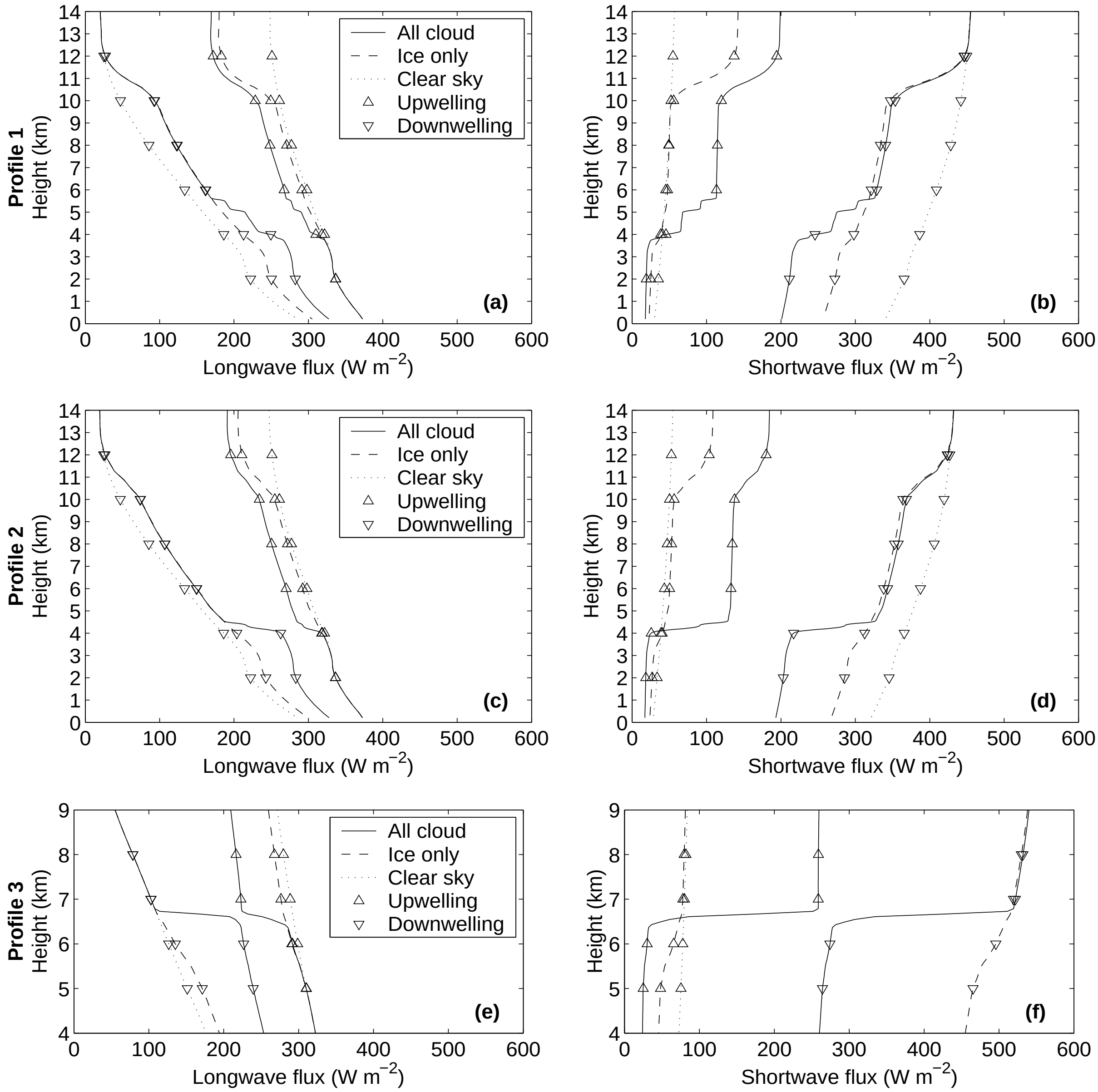

Figure 3.5: Upwelling and downwelling long-wave and short-wave fluxes calculated for the three profiles shown in Figs. 3.2–3.4. The different line styles correspond to calculations with both ice and liquid cloud present (solid lines), with only ice cloud present (dashed lines) and with no cloud present (dotted lines).

effects of ice and liquid.

The solar zenith angles used in the short-wave calculations were 69.5°, 70.5° and 64.9° for profiles 1, 2 and 3 respectively. In accordance with the radar and lidar observations of this study, in layers where both ice and liquid water were present they were assumed to be mixed homogeneously for the purposes of calculating the layer single-scattering properties. In the first two profiles the vertical resolution of the calculations was variable; in the vicinity of the liquid water layers it matched the 15 m resolution of the data, while elsewhere in the troposphere it varied between 50 m and 200 m. In the third profile the 60 m resolution of the data was used throughout the troposphere. We compare calculations performed with (a) clear skies, (b) only the ice phase present, (c) only the liquid phase present and (d) both the ice and liquid water phases present.

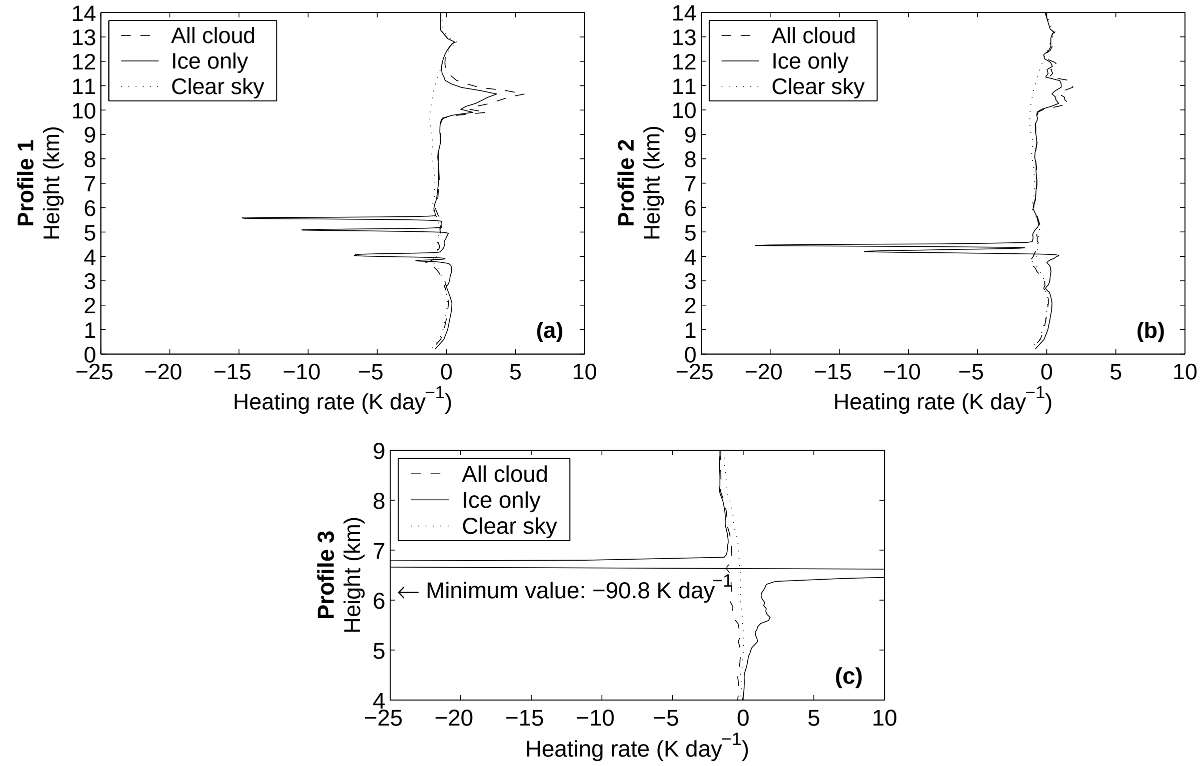

Figure 3.6: Heating rate profiles calculated from the fluxes in Fig. 3.5.

The liquid and ice water paths and visible optical depths of the three profiles are listed in Table 3.1; it can be seen that the relative amount of supercooled liquid water increases through profiles 1 to 3. The resulting upwelling and downwelling broad-band fluxes are plotted versus height in Fig. 3.5, and the corresponding heating-rate profiles, calculated from the divergences of these fluxes, are depicted in Fig. 3.6. Table 3.2 lists the values of albedo, outgoing long-wave radiation, reflected short-wave radiation and net absorbed radiation for each case. To see more easily the overall effect of the various scenarios on the radiation budget, Table 3.3 lists the changes in these parameters that occur when ice, liquid, and both ice and liquid are added to the clear sky profiles.

In profile 1 the liquid water was present in four individual layers, although the the total liquid water path (LWP) was only 5.4 g m^{-2}, five times less than the ice water path (IWP). Comparing the 'all cloud', 'ice only' and 'clear sky' profiles in Fig. 3.5a we see that the liquid water dominated the radiative properties of the mid-level cloud in the long-wave, where the ice had very little effect. This is indeed what would be expected from the much larger backscatter coefficients of the liquid water layers compared to the ice. The peak cooling rate of the uppermost layer (due to long-wave emission to space) was around 15 K day^{-1} (Fig. 3.6a), although concentrated in a very thin layer. The outgoing long-wave radiation (OLR), however, was influenced most strongly by the cold, high cirrus, which had the effect of reducing OLR by 65.7 W m^{-2} from its clear-sky value (see Table 3.3). The liquid water layers beneath caused an additional modest reduction of 10.1 W m^{-2} in this parameter.

The radiative effect of the liquid water in the short-wave was much greater; the increase in reflected short-wave radiation due to liquid water alone was 108.7 W m^{-2} (compared to the clear-sky value), over four times greater than the corresponding decrease in OLR. Consequently, there was a quite substantial decrease in net absorbed radiation of 83.5 W m^{-2}. In contrast, the long-wave and short-wave effects of the ice cloud alone tended to cancel out (by virtue of the predominantly colder temperatures of the ice cloud), and the change in net absorbed radiation from the clear-sky value was only 18.2 W m^{-2}. With both ice and liquid water in the profile the decrease in net absorbed radiation was 63.7 W m^{-2}. Hence the high-level cirrus acted to partially offset the radiative effect of the liquid water layers beneath.

The results for profile 2 are broadly similar to those for profile 1. A little more liquid water was concentrated in a double-peaked layer in a profile containing somewhat less ice, and consequently the relative importance of liquid water was greater. The effect of liquid water alone was to decrease the net absorbed radiation by 88.4 W m^{-2}, compared with a decrease of 12.8 W m^{-2} for ice alone.

The liquid water in profile 3 was concentrated in a single layer at -23°C, with an LWP of 11.6 g m^{-2} and visible optical depth of nearly 4. The ice (with an IWP of 8.9 g m^{-2}) was almost entirely beneath the liquid water, and consequently the liquid water dominated both the short-wave and long-wave properties of the cloud. The liquid water had the effect of decreasing OLR by 56.1 W m^{-2} while increasing the reflected short-wave radiation by 190.0 W m^{-2} (nearly a factor of four increase in albedo). The decrease in net absorbed radiation of 133.9 W m^{-2} was thus much larger than the 10.0 W m^{-2} decrease due purely to ice. Fig. 3.6c shows that the peak cooling rate near the top of the liquid water layer was 90.8 K day^{-1}, clearly large enough to drive convective overturning, explaining the cellular nature of the cloud observed during the experiment. This is similar to the value of around 80 K day^{-1} calculated by Heymsfield *et al.* (1991) for the top of -30°C altocumulus cloud.

As for all clouds, the radiative effect of the supercooled liquid water layers is of opposite sign in the long- and the short-wave, but, in these examples at least, the short-wave effect was 3–5 times stronger. Thus, by their increased reflection of solar radiation back to space, these clouds have an overall cooling effect in much the same way as stratocumulus. In each of these profiles the effect of liquid water on the net absorbed radiation was considerably more than the ice contribution, even when ice cloud was present above. However, the greatest cirrus optical depth considered was only 0.75 (in Profile 1); presumably much thicker cirrus could significantly reduce the effect of the liquid water on the top-of-atmosphere radiation parameters.

3.5 Conclusions

In the CLARE'98 experiment supercooled liquid water clouds were observed between -7°C and -23°C. They occurred in the form of layers 100–200 m thick above or embedded within thicker ice clouds, and were easily identifiable from their very strong lidar return, while the radar return was dominated by the contribution from the larger ice particles. As shown by Hogan *et al.* (2003), on 20 October 1998 gravity waves were believed to be initially responsible for the vertical velocities that caused the condensation of liquid water, and *in situ* sampling at the crests of these waves found liquid water contents of 0.05 g m^{-3} and effective radii of around 2 μm. In both cases the optically thick liquid water layers at cloud top then emitted strongly to space in the infrared, and the consequent cooling (Fig. 3.6) generated convective overturning sufficient to sustain the liquid water. Ice falling beneath the uppermost layer presumably then depleted the ice nucleus concentration at that altitude enabling them to persist for longer periods. The available *in situ* data in the more mature supercooled clouds found liquid water contents of 0.1–0.2 g m^{-3} and effective radii of 3–5 μm.

Radiation calculations have shown that, when present, supercooled liquid water can easily have a larger effect on the radiation field than the ice. Because supercooled liquid clouds do not occur at temperatures colder than around -35°C, their short-wave effect invariably outweighs the long-wave effect (by a factor 3–5 in the cases discussed in section 3.4). Thus they have a net cooling effect on climate, and in this way are rather similar to stratocumulus (Heymsfield *et al.* 1991). The long- and short-wave effects of ice clouds at colder temperatures, on the other hand, tend to be more similar in magnitude.

There are several reasons why these layers are very unlikely to be represented realistically in current forecast and climate models. Firstly, many microphysics parameterizations have a minimum temperature below which liquid water cannot form (e.g. -9°C for Moss and Johnson 1994, -15°C for Smith 1990). Secondly, the vertical resolution of current models in the mid-troposphere is usually around 500 m, much thicker than the typical supercooled cloud thicknesses observed by lidar. Finally, the vertical velocities responsible for the formation and persistence of supercooled liquid seem to be very much associated with sub-gridscale phenomena such as cellular convection or gravity waves, rather than the large-scale ascent that might be represented by the gridbox-mean vertical velocity.

In order to evaluate the broader radiative importance of these clouds it is necessary to determine how often they occur. In the next chapter, supercooled water clouds are identified in many months of data from a ground-based lidar at Chilbolton. To determine their full importance for climate, measurements are needed on a global scale. The proposed spaceborne cloud lidar and radar would be ideally suited to this task, and in a subsequent chapter, data from LITE (the Lidar Inspace Technology Experiment) are used to demonstrate the identification of supercooled liquid water from space. A spaceborne cloud radar alone, while having the capacity to make excellent measurements of ice water content even in attenuating conditions for lidar (Liu and Illingworth 2000), may not be able to accurately constrain the radiation budget in some cases because of its inability to detect supercooled water.

References

Battan, L. J., 1973: *Radar observation of the atmosphere.* University of Chicago Press.

Brown, P. R. A., 1993: Measurement of the ice water content of cirrus using an evaporative technique. *J. Atmos. Oceanic Tech.,* **10,** 579–590.

Brown, P. R. A., and Francis, P. N., 1995: Improved measurements of the ice water content in cirrus using a total-water probe. *J. Atmos. Oceanic Tech.,* **12,** 410–414.

Edwards, J. M, and Slingo, A., 1996: Studies with a flexible new radiation code. 1: Choosing a configuration for a large scale model. *Q. J. R. Meteorol. Soc.,* **122,** 689–719.

ESA (European Space Agency), 1999a: CLARE'98 Cloud Lidar & Radar Experiment. ESA Report WPP-170, ESTEC, Noordwijk, The Netherlands, 239 pp.

ESA (European Space Agency), 1999b: Earth Radiation Mission. ESA Report SP-1233(3)—The four candidate Earth Explorer Core Missions, ESTEC, Noordwijk, The Netherlands, 191 pp.

Foot, J. S., 1988: Some observations of the optical properties of clouds. 2: Cirrus. *Q. J. R. Meteorol. Soc.,* **114,** 145–164.

Francis, P. N., Hignett, P., and Macke, A., 1998: The retrieval of cirrus cloud properties from aircraft multi-spectral reflectance measurements during EUCREX'93. *Q. J. R. Meteorol. Soc.,* **124,** 1273–1291.

Francis, P. N., Flentje, H., Pelon, J., and Testud, J., 1999: An analysis of the airborne broad-band radiometer measurements collected during CLARE'98. CLARE'98 Cloud Lidar & Radar Experiment, ESA Report WPP-170, ESTEC, Noordwijk, The Netherlands, 225–229.

Fu, Q., and Liou, K. N., 1993: Parameterization of the radiative properties of cirrus clouds. *J. Atmos. Sci.,* **50,** 2008–2025.

Gardiner, B. A., and Hallett, J., 1985: Degradation of in-cloud forward scattering spectrometer probe measurements in the presence of ice particles. *J. Atmos. Sci.,* **2,** 171–180.

Gregory, D., and Morris, D., 1996: The sensitivity of climate simulations to the specification of mixed phase clouds. *Climate Dynamics,* **12,** 641-651.

Heymsfield, A. J., Miloshevich, L. M., Slingo, A., Sassen, K., and Starr, D. O'C., 1991: An observational and theoretical study of highly supercooled altocumulus. *J. Atmos. Sci.,* **48,** 923–945.

Hogan, R. J., and Goddard, J. W. F., 1999: Calibration of the ground-based radars during CLARE'98. CLARE'98 Cloud Lidar & Radar Experiment, ESA Report WPP-170, ESTEC, Noordwijk, The Netherlands, 63–67.

Hogan, R. J., and Illingworth, A. J., 1999: The potential of spaceborne dual-wavelength radar to make global measurements of cirrus clouds. *J. Atmos. Oceanic Tech.,* **16,** 518–531.

Hogan, R. J., Illingworth, A. J., and Sauvageot, H., 2000: Measuring crystal size in cirrus using 35- and 94-GHz radars. *J. Atmos. Oceanic Tech.,* **17,** 27–37.

Hogan, R. J., Francis, P. N., Flentje, H., Illingworth, A. J., Quante, M., and Pelon, J., 2003: Characteristics of mixed-phase clouds. 1: Lidar, radar and aircraft observations from CLARE'98. *Q. J. R. Meteorol. Soc.,* **129,** 2089–2116.

Hu, Y. X., and Stamnes, K., 1993: An accurate parameterization of the radiative properties of water clouds suitable for use in climate models. *J. Climate,* **6,** 728–742.

Illingworth, A. J., R. J. Hogan, A. C. A. P. van Lammeren, D. P. Donovan, F. H. Berger, T. Halecker, C.-L. Liu, A. Feijt and H. I. Bloemink, 2000: Quantification of the synergy aspects of the Earth Radiation Mission, Final report, ESTEC Contract 13167/98/NL/GD.

Intrieri, J. M., Stephens, G. L., Eberhart, W. L., and Uttal, T., 1993: A method for determining cirrus cloud particle sizes using lidar and radar backscatter techniques. *J. Appl. Meteorol.,* **32,** 1074–1082.

Klett, J. D., 1985: Lidar inversion with variable backscatter/extinction ratios, *J. Atmos. Opt., 24,* 1638–1643.

Knollenberg, R. G., 1970: The optical array: An alternative to scattering for airborne particle size determination. *J. Appl. Meteorol.,* **9,** 86–103.

Kosarev, A. L., and Mazin, I. P., 1989: Empirical model of physical structure of the upper level clouds of the middle latitudes. In *Radiation properties of cirrus clouds,* pp. 29–52, Nauka, Moskow.

Li, Z.-X., and Le Treut, H., 1992: Cloud-radiation feedbacks in a general circulation model and their dependence on cloud modelling assumptions. *Climate Dynamics,* **7,** 133–139.

Liebe, H. J., 1985: An updated model for millimeter-wave propagation in moist air. *Radio Sci.,* **20,** 1069–1089.

Liu, C.-L., and Illingworth, A. J., 2000: Towards more accurate retrievals of ice water content from radar measurements of clouds. *J. Appl. Meteorol.,* **39,** 1130-1146.

Macke, A., Mueller, J., and Raschke, E., 1996: Single scattering properties of atmospheric ice crystals. *J. Atmos. Sci.*, **53,** 2813–2825.

Mörl, P., Reinhardt, M. E., Renger, W., and Schellhase, R., 1981: The use of the airborne lidar system 'ALEX F1' for aerosol tracing in the lower troposphere. *Contr. Atmos. Phys.,* **54,** 401–410.

Moss, S. J., and Johnson, D. W., 1994: Aircraft measurements to validate and improve numerical model parametrizations of ice to water ratios in clouds. *Atmos. Res.,* **34,** 1–25.

Pelon, J., Flamant, P. H., and Meissonnier, M., 1990: The French airborne backscatter lidar LEANDRE. 1: Conception and operation. *Proc. 15th Int. Laser Radar Conf.,* **36,** Tomsk.

Quante, M., Danne, O., Lemke, H., Milferstädt, D., and Raschke, E., 1998: The GKSS 94-GHz cloud radar: system description and potential contributions in support of the Earth Radiation Mission. *ESA Report EWP-1968*, 75–80, ESTEC, Noordwijk, The Netherlands.

Quante, M., Lemke, H., Flentje, H., Francis, P. N., and Pelon, J., 2000: Boundaries and internal structure of mixed phase clouds as deduced from ground-based 95-GHz radar and airborne lidar measurements. *Phys. Chem. Earth,* **25,** 889–895.

Sekelsky, S. M., Ecklund, W. L., Firda, J. M., Gage, K. S., and McIntosh, R. E., 1999: Particle size estimation in ice-phase clouds using multifrequency radar reflectivity measurements at 95, 33 and 2.8 GHz. *J. Appl. Meteor.,* **38,** 5–28.

Slingo, A., and Schrecker, H. M., 1982: On the shortwave radiative properties of stratiform water clouds. *Q. J. R. Meteorol. Soc.,* **108,** 407–426.

Smith, R. N. B., 1990: A scheme for predicting layer clouds and their water content in a general circulation model. *Q. J. R. Meteorol. Soc.,* **116,** 435–460.

Sun, Z., and Shine, K. P., 1995: Parameterization of ice cloud radiative properties and its application to the potential climatic importance of mixed-phase clouds. *J. Climate,* **8,** 1874–1888.

Tremblay, A., Glazer, A., Yu, W., Benoit, R., 1996: A mixed-phase cloud scheme based on a single prognostic equation. *Tellus A,* **48,** 483–500.

Wilson, D. R., and Ballard, S. P., 1999: A microphysically based precipitation scheme for the UK Meteorological Office Unified Model. *Q. J. R. Meteorol. Soc.,* **125,** 1607–1636.

Chapter 4

Algorithm for detection of supercooled water and climatology from Chilbolton and Cabauw

Summary. In this chapter, 18 months of near-continuous lidar data from two mid-latitude locations were analysed to estimate the frequency of occurrence of such clouds as a function of temperature. An algorithm was developed that uses the integrated backscatter to identify liquid water clouds with a visible optical depth of greater than 0.7 (i.e. those that scatter more than half of the incident radiation), and was found to compare favourably with microwave radiometer measurements of liquid water path. From data taken with a lidar pointing at 5° from zenith, the frequency of supercooled liquid water layers over Chilbolton in Southern England was found to fall steadily with temperature; 27% of clouds between -5°C and -10°C were found to contain significant liquid water, falling to only 6% of clouds observed between -25°C and -30°C. The horizontal extent of the layers typically ranged between 20 and 70 km. When the lidar was pointed directly at zenith, specular reflection by horizontally aligned plate crystals was found to bias the statistics between -10°C and -20°C. The importance of supercooled liquid water clouds in the radiation budget is reduced when thick ice clouds are present above them, so we then used simultaneous cloud radar data to estimate the optical depth of any cloud above. It was found that around 30% of supercooled liquid water clouds with temperatures between 0°C and -20°C had ice above with a visible optical depth in excess of 0.5, falling to 10% between -20°C and -30°C. Given the substantial optical depth of the supercooled water itself, we conclude that in the majority of cases when supercooled water is present, it will dominate the radiative properties of the cloud profile. Finally, we compared the occurrence of supercooled liquid clouds with the amounts found in the models of the UK Met Office and the European Centre for Medium Range Weather Forecasts (ECMWF). Both models were found to produce too much supercooled liquid at warmer temperatures and too little at colder temperatures (with virtually none being simulated below -20°C), although the occurrence of supercooled cloud was far higher in the ECMWF model than the Met Office model. The observations in this paper are limited to one climatic zone but the forthcoming spaceborne lidars will be able to extend these comparisons to the whole globe.

4.1 Introduction

In the previous chapter it was shown that supercooled liquid water clouds can occur in the form of thin but radiatively significant layers, around 150 m thick, that are distinctly visible to lidar due to their very high backscatter coefficient. By contrast, the echo from cloud radar tends to be dominated by the contribution from the larger but much less numerous ice particles. In this paper we use around 8 months of near-continuous data taken by a 905-nm Vaisala lidar ceilometer located at Chilbolton, England, and 10 months of data from an identical instrument at Cabauw, The Netherlands, to estimate the frequency of occurrence of supercooled clouds as a function of temperature. These instruments do not have polarization capability, and although depolarization ratio is perhaps the most well-known method to detect cloud particle phase remotely (Sassen 1991), the high backscatter coefficient of the layers combined with their rapid extinction of the lidar signal makes them quite easy to detect using a simple backscatter lidar. An algorithm is developed which utilizes the integrated backscatter coefficient through the candidate layer; due to the approximately constant extinction-to-backscatter ratio of distributions of liquid water droplets with median diameters in the range 5–50 μm, this can be used to impose a lower limit on the optical depths that are detected. Importantly, the Vaisala instrument is able to operate continuously in all weather conditions, an essential consideration if a representative climatology is to be built up. Of course, there may be considerable regional variability to the characteristics of mixed-phase clouds, but this chapter demonstrates a methodology that could be applied to other lidars, both from the ground and from space. It should be noted that a simpler algorithm was used by Illingworth *et al.* (2000) on data from the same instrument, but involved arbitrary backscatter thresholds so could not be interpreted in terms of optical depth and therefore the climatology obtained could not be compared quantitatively to models.

Radiative transfer calculations were performed in the previous chapter to estimate the radiative importance of the supercooled liquid water layers observed and it was found that in each profile analysed the effect of the liquid water on the net top-of-atmosphere radiation was greater than that of the ice. In principle, however, thick cirrus could swamp the radiative signature of the liquid-phase cloud beneath. The thickest cirrus considered in the previous chapter had an optical depth of 0.78, and caused a reduction in outgoing long-wave radiation of 65.7 W m^{-2}, much larger than the 25.2 W m^{-2} due to the liquid water below. However, the increase in reflected short-wave radiation due to the ice was less than that due to the liquid water, with the result that the liquid water still had a significantly greater effect on the *net absorbed* radiation than the ice (-83.9 W m^{-2} as opposed to -18.2 W m^{-2}). To determine how often thick cirrus occurs in conjunction with supercooled clouds, we use the vertically pointing 94-GHz *Galileo* radar at Chilbolton, which also operates near-continuously, to estimate the optical depth of any cirrus whenever the lidar detects a supercooled liquid water cloud.

Several lidar studies of cirrus (Gibson *et al.* 1977; Platt *et al.* 1978; Sassen 1984; Thomas *et al.* 1990) have found cases of ice clouds that exhibit enhanced backscatter when viewed from zenith, up to a factor of 20 higher than the backscatter measured when the lidar is pointed only a few degrees to the side. This can be explained by the presence of horizontally oriented plate crystals that undergo specular reflection when viewed from directly below. These are the same crystals that reflect sunlight preferentially in particular directions to produce certain optical phenomena. From the angular dependence of the backscatter, Thomas *et al.* (1990) estimated the maximum tilt of the crystals from the horizontal plane to be around 0.3°. Unlike in the case of supercooled water layers, the enhanced backscatter due to aligned plates is not accompanied by a strong increase in extinction, but there is still a danger that specular reflection could be mistaken for supercooled water. We therefore use data taken at 5° from zenith to determine the frequency of occurrence of liquid water layers, and compare these results to data taken at zenith to estimate the prevalence of specular reflection in ice clouds. It should be noted that the specular component of reflection from plate crystals is not depolarized, so depolarization ratio does not provide a means to distinguish specularly reflecting ice crystals from liquid water droplets.

In section 4.2 the lidar and radar instruments are described, including details of their calibration.

In section 4.3 we describe the algorithm used to diagnose the presence of liquid water with lidar and the methodology for using simultaneous radar data to estimate the optical depth of any ice cloud above. The results are then presented in section 4.4, including comparison of the observed occurrence of supercooled water clouds with the amounts in the models of UK Met Office model and the European Centre for Medium Range Weather Forecasts (ECMWF). The results in this chapter have been published (Hogan *et al.* 2003c).

4.2 Instrumentation

The main instrument used in this chapter is the 905-nm Vaisala CT75K lidar ceilometer, which has a range gate spacing of 30 m and obtains improved sensitivity, despite its low power, by integrating for 30 s. The Chilbolton lidar has operated continuously since January 1997, except for a few periods off-line for maintenance. It was originally set up in a zenith-pointing configuration, but in December 1999 was adjusted to point at 5° from zenith; data both with and without contamination from specular reflection are therefore available. We also use data from an identical instrument operating at 5° from zenith at Cabauw, The Netherlands, between October 2001 and July 2002. The lidars have been calibrated by integrating the raw attenuated backscatter coefficient up through completely attenuating stratocumulus (O'Connor *et al.* 2003). Theoretically this integral should be equal to $(2\eta k)^{-1}$, where η is the multiple-scattering factor and k is the extinction-to-backscatter ratio (Platt 1973). In the next section it is shown that these parameters can be assumed constant in the type of clouds under consideration.

The optical depth of the ice clouds above the supercooled liquid water is estimated using the 94-GHz *Galileo* radar at Chilbolton. This instrument has operated near-continuously in a vertically pointing configuration between November 1998 and October 2000. Calibration has been performed regularly by comparison with the 3-GHz radar at Chilbolton, as described by Hogan *et al.* (2003a), and is believed to be accurate to better than 1.5 dB. It was found that the power emitted by the instrument decreased steadily by 11 dB in these two years of operation. The last 94-GHz data used in this chapter, from October 2000, had a minimum detectable radar reflectivity of around -39 dBZ at 1 km.

4.3 Method

4.3.1 Objective diagnosis of the presence of supercooled liquid water

In this section we describe the algorithm used to detect the presence of supercooled water. The technique essentially locates highly reflective layers in the lidar imagery that, on the basis of the observations by Hogan *et al.* (2003b), have a backscatter coefficient that is too high to be likely to be caused by ice alone. By utilizing the integrated backscatter coefficient, it is possible to accurately specify the optical depth that will trigger the algorithm. This approach was first suggested by Platt (1973) and was used by him in the study of clouds in numerous subsequent papers.

The lidar measures attenuated backscatter coefficient β', which is related to true backscatter coefficient β by

$$\beta'(z) = \beta(z)\, e^{-2\eta\tau(z)}, \tag{4.1}$$

where $\tau(z)$ is the optical depth of the atmosphere at 905 nm between the instrument and the point of observation at height z. This equation follows Platt (1973) in its representation of multiple scattering by a single factor η, which can take a value between 0.5 and 1 depending on the parameters of the lidar and the nature of the scatterers in the cloud.

In each lidar profile, the algorithm determines the height of the highest value of β' and then calculates the integrated backscatter through this 'candidate' liquid water layer, γ_w, defined by

$$\gamma_w = \int_{z_1}^{z_2} \beta' \, dz, \tag{4.2}$$

where z_1 is 100 m below the height of the highest β' and z_2 is 200 m above the height of the highest β'. It is our experience that, due to their strong attenuation, individual liquid water layers tend to occupy no more than 300 m of a lidar profile, and that z_1 and z_2 defined in this way encapsulate liquid water layers most effectively. Noting that extinction coefficient α is equal to $d\tau/dz$, and assuming the extinction-to-backscatter ratio, $k = \alpha/\beta$, to be constant through the cloud, we can change variables and write

$$\begin{aligned} \gamma_w &= \frac{1}{k} \int_{\tau_1}^{\tau_1+\tau_w} e^{-2\eta\tau} d\tau \\ &= \frac{1}{2\eta k} e^{-2\eta\tau_1} \left(1 - e^{-2\eta\tau_w}\right), \end{aligned} \tag{4.3}$$

where τ_w is the optical depth of the candidate liquid water layer and τ_1 is the optical depth of the atmosphere from the surface to z_1.

In the simple case of the lidar having an unobscured view of the liquid water layer ($\tau_1 \simeq 0$) and the layer being optically thick ($\tau_w \to \infty$), (4.3) reduces to $\gamma_w = (2\eta k)^{-1}$. Using complex angular momentum theory at a wavelength of 1.06 μm, Pinnick *et al.* (1983) calculated that for droplet distributions typically found in liquid water clouds, k is approximately constant at 18.2 sr. Using Mie theory at 905 nm and distributions with median volume diameters in the range 5–50 μm, we find that k is approximately constant at 18.75 sr. Using the code of Eloranta (1998) and realistic droplet size distributions observed at a range of at least 3 km, we calculate that for the CT75K lidar beam divergence (0.75 mrad half-angle) and field-of-view (0.66 mrad half-angle), η is approximately constant at 0.7 ± 0.04. Therefore, γ_w in optically thick liquid water clouds is around 0.038 sr^{-1}.

We specify that the supercooled liquid water clouds detected by the algorithm should have an optical depth τ_w greater than 0.7; i.e. that over half of the radiation incident normally on the cloud layer should be scattered. Thus, if it is still assumed that $\tau_1 \simeq 0$, then from (4.3) the condition for such a cloud to be detected is $\gamma_w > 0.024$ sr^{-1}. The fraction of clouds that contain a liquid water layer in any given temperature interval may then be calculated by dividing the time for which γ_w exceeds this threshold and lies in the specified temperature interval, by the total time that any cloud is detected in this temperature range.

In reality there may be significant optical depth beneath a liquid cloud layer, most commonly in the case of ice virga beneath an altocumulus layer, but aerosol attenuation could also be a factor. If uncorrected this could lead to an underestimate of the fraction of clouds containing a layer due to the reduction in measured γ_w. Since k is much less certain in ice than in liquid, we cannot reliably perform a gate-by-gate correction for attenuation. Instead we simply remove cloudy pixels that have an optical depth beneath them high enough that they could never be diagnosed as being a liquid water layer by the criterion of $\gamma_w > 0.024$ sr^{-1}. The cloud below the layer is assumed to have a k equivalent to the liquid water value; this will sometimes remove too much cloud and sometimes too little, but as it is also a fairly typical value for ice, any bias should be small. This procedure removes around 20% of the cloudy pixels.

4.3.2 Examples of mixed-phase clouds observed by ground-based radar, lidar and microwave radiometer

Figures 4.1 and 4.2 show cases of supercooled liquid water observed at Chilbolton. The first is from 6 August 1999 and depicts 12-h time-height sections of radar and lidar data. Superimposed on the

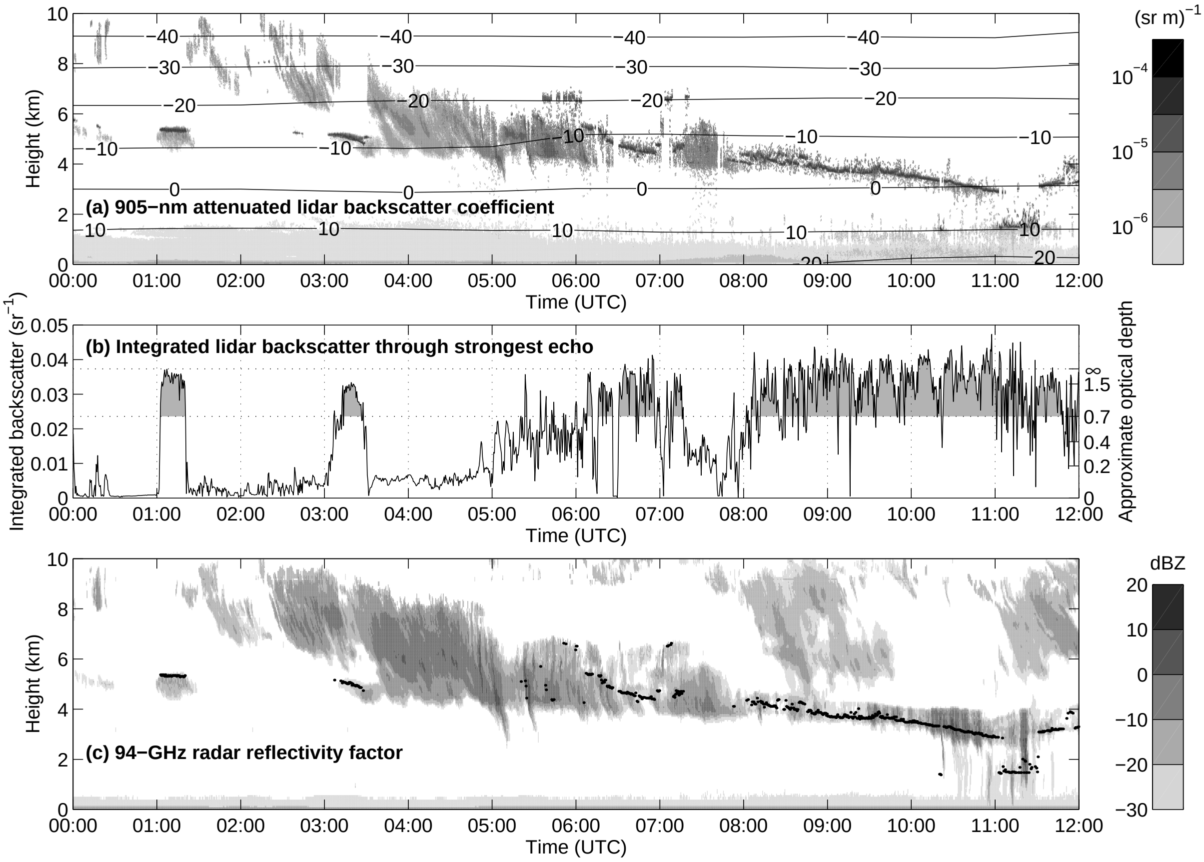

Figure 4.1: Example of mixed-phase cloud detection on 6 August 1999 at Chilbolton: (a) 12-h time-height section of attenuated lidar backscatter coefficient, β', overlaid by temperature from the UK Met Office model in °C; (b) integrated attenuated backscatter coefficient in a 300 m window around the location of the highest β'; (c) attenuation-corrected 94-GHz radar reflectivity factor. The shaded areas of (b) indicate the presence of a liquid water layer with an optical depth of more than 0.7, the location of which is shown by the black points in (c).

lidar image are temperature contours from the mesoscale version of the operational Met Office Unified Model. The model dataset is hourly, composed of the 6-hourly analyses followed by the intervening hourly forecasts. In the lowest kilometre the lidar detects boundary-layer aerosol, while the radar echo is contaminated by returns from the ground and insects. Above this, at temperatures between +10°C and −20°C, a number of thin but highly reflective layers, believed to be composed of liquid water, are apparent in the lidar signal. They are very similar in appearance to the layers observed by Hogan *et al.* (2003b), which depolarization measurements and *in situ* sampling confirmed to be composed of liquid water. For most of the time in Fig. 4.1 when a layer was observed at temperatures below 0°C, the radar detected ice falling beneath it. Figure 4.1b depicts the integrated backscatter γ_w in a 300 m vertical window encompassing the strongest echo, with the values above the detection threshold of 0.024 sr^{-1} shaded. The location of the diagnosed liquid water layer is shown by the black points in Fig. 4.1c, and in general matches the layers that might be identified subjectively on inspection of Fig. 4.1a.

The second case is from 10 November 2001, when the clouds were almost entirely composed of liquid water and the radar (not shown) did not detect any cloud. The integrated backscatter in Fig. 4.2b shows that the cloud was, in general, optically thick. Figure 4.2c shows concurrent measurements of liquid water path by a dual-wavelength microwave radiometer at 22.2 GHz and 28.8 GHz. The times

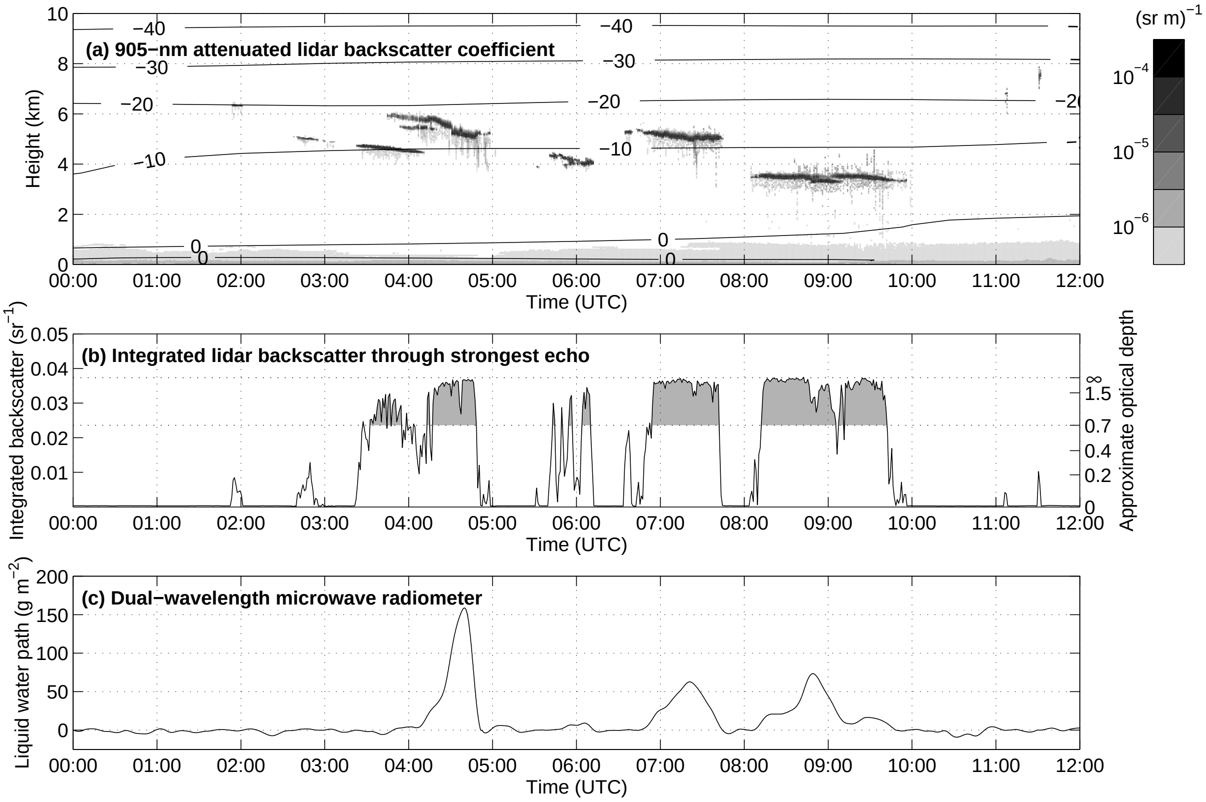

Figure 4.2: Supercooled water detection on 10 November 2001: (a) attenuated backscatter coefficient, (b) the approximate optical depth of the layer, as in Fig. 4.1, and (c) liquid water path retrieved using a dual-wavelength microwave radiometer.

that liquid water was detected agree well with the lidar measurements, with values reaching 150 g m^{-2}. However, it is interesting that there are optically significant liquid water clouds apparent in the lidar data at around 03:45 and 08:00 UTC that have very low liquid water paths and so are scarcely detected by the microwave radiometer. This is consistent with the finding in the previous chapter that supercooled liquid clouds with a liquid water path as low as 10 g m^{-2} can still have a significant radiative effect.

4.3.3 Estimating the optical depth of ice cloud

At Chilbolton, the visible extinction coefficient (α) of ice clouds may be estimated from the effective radar reflectivity factor (Z) measured by the 94-GHz cloud radar. This can then be integrated in height to estimate the optical depth (τ) of any ice cloud above the supercooled liquid water observed by the lidar. The first step is to correct the reflectivity values for attenuation. Correction of gaseous attenuation is performed using the temperature and humidity profile held over Chilbolton from the mesoscale version of the Met Office model, coupled with the line-by-line model for millimetre-wave attenuation of Liebe (1985). The two-way liquid water attenuation at 94 GHz is less than 0.01 dB (g m^{-2})$^{-1}$, so for the values of liquid water path shown in Fig. 4.2 and in the first table of the previous chapter, the attenuation rarely reaches 1 dB and is often less than 0.1 dB. Of course, detection of supercooled liquid water by lidar implies that no thicker liquid water cloud is present below, so we assume that liquid water attenuation is negligible.

A relationship between Z and α has been derived from a total of around 14 hrs of ice size spectra measurements in mid-latitude cirrus between $-2°$C and $-57°$C by the Met Office C-130 aircraft, taken

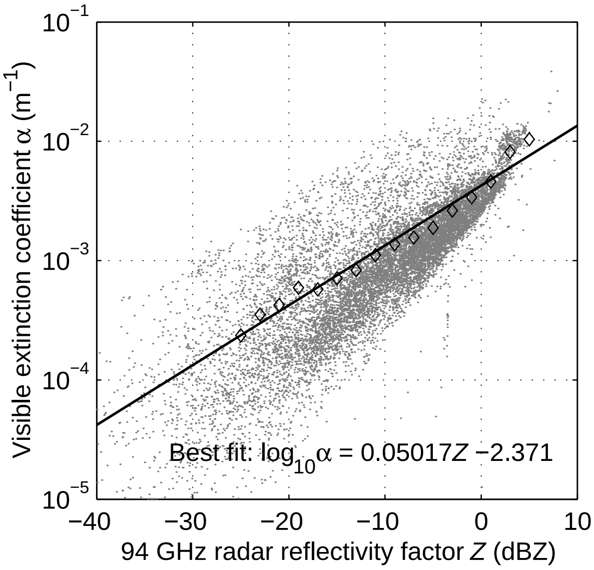

Figure 4.3: Scatterplot of Z versus α derived from the EUCREX aircraft dataset. The diamonds depict the linear mean α in each 2 dBZ range of Z, and the solid line is the regression to the diamonds.

predominantly during the European Cloud Radiation Experiment (EUCREX). It should be stressed that the ice under consideration in this chapter is exclusively *above* the supercooled water, so is unlikely to be affected by it microphysically, justifying the use of a general cirrus dataset. Indeed, in the 20 October 1998 case of the previous chapter, most of the ice optical depth was in the cirrus which had a base 3 km higher than the highest liquid water layer.

Radar reflectivity factor is calculated using the same approach as Brown *et al.* (1995) and Hogan and Illingworth (1999); the ice particles observed by the 2D probes of the C-130 (spanning the diameter range 25–6400 μm) are approximated as spheres with a mass given by the relationship of Brown and Francis (1995) and a diameter, D_{m}, equal to the mean of the maximum dimensions of the particle measured parallel and perpendicular to the photodiode array of the probe. Then Mie theory is applied. Extinction coefficient is calculated directly from the observed cross-sectional area of the crystals assuming geometric optics. To account for the under-counting of the small particles by the 2D cloud probe, we take a similar approach to Francis *et al.* (1998) and fit a gamma distribution to the lower end of each size spectrum. The gamma distribution is constrained to have a modal diameter of 6 μm, to have the same concentration of 100-μm particles as observed, but twice as many 25-μm particles. This increases the ice water content contained in the particles smaller than 90 μm by around a factor of 2.5, thereby correcting for the average difference that McFarquhar and Heymsfield (1997) found when they compared the 2D cloud probe to the video ice particle sampler.

The data are shown in Fig. 4.3, where each point represents a 5-s aircraft sample. Simple regressions in logarithmic space can result in biased retrievals when the scatter of the data is large. To avoid this problem we first compute the linear mean of α in each 2 dB radar reflectivity interval between -25 and $+5$ dBZ (shown by the diamonds) and then perform a linear regression in logarithmic space to these means. The resulting best-fit line has the form

$$\log_{10}(\alpha) = 0.05017\,Z - 2.371, \tag{4.4}$$

where α is in m^{-1} and Z in dBZ. The scatter of the data points is due principally to variations in mean particle size and represents an rms error on a retrieval of α of around $+200\%/-70\%$ for $Z \simeq -20$ dBZ, falling steadily to $+40\%/-30\%$ for $Z \simeq 0$ dBZ. In integrating retrieved extinction coefficients with height to obtain optical depth, one might expect the increase in mean size from cloud top to cloud base to introduce an independence in the errors in α at different altitudes, resulting in a somewhat more accurate estimate of optical depth. Nonetheless, we test the sensitivity to the scatter of the data by also calculating the optical depths using expressions that represent one standard deviation above and below the best-fit line of (4.4).

The principal remaining uncertainty lies in the choice of diameter in the Mie calculations to determine Z. The diameter D_m used here is commonly around 25% larger than the 'equivalent area' diameter used in the previous chapter, and results in lower values of Z for the same particle mass because of the greater departure from Rayleigh scattering. This in turn leads to the retrieval of a larger value of extinction coefficient for a given measurement of Z. In consequence, the optical depth of cirrus is more likely to be overestimated than underestimated, resulting in a conservative estimate of how often any supercooled water clouds observed by the lidar beneath the cirrus is radiatively important.

4.4 Results

4.4.1 Frequency of occurrence of supercooled water layers

We first analyse the data collected at Chilbolton when the lidar was pointing 5° from zenith, which consists of essentially the whole of 2000, barring 12 January to 26 April when the instrument was taken off-line for repairs. In total more than 700,000 30-s rays have been processed, equivalent to 248 days of continuous observation. The results are shown in Fig. 4.4. Panel a shows the fraction of the dataset for which the instrument observed any cloud in each 5°C temperature interval between −50°C and 0°C. Hourly temperature profiles over Chilbolton were taken from the mesoscale version of the Met Office model. Pixels were defined to be cloudy if the lidar backscatter coefficient was 7.5×10^{-7} sr^{-1} m^{-1} or greater (the data were digitized in units of 2.5×10^{-7} sr^{-1} m^{-1}). To avoid contamination by boundary-layer aerosol, only data above 2 km were considered. An objective method was devised to 'clean up' the clear-air noise occasionally produced by this instrument. It can be seen that, except for the warmest bin, the occurrence of cloud in each 5°C temperature interval was less than 5% and decreased with decreasing temperature. This is appreciably less than the true mid-level cloud occurrence over Chilbolton of around 20% (Hogan *et al.* 2001), because of the problem of lidar obscuration by lower level clouds, particularly stratocumulus.

Figure 4.4b shows the fraction of the observed cloud (i.e. the fraction of cloudy rays) in each 5°C interval that contained a supercooled liquid water layer. The error bars were calculated assuming Poisson statistics, with every individual continuous layer being regarded as an independent event. Gaps of up to 10 mins were permitted in layers for them still to be regarded as continuous, to allow for occasional obscuration by boundary-layer cumulus. As one might expect, the fraction of clouds containing a supercooled liquid water layer decreased with decreasing temperature; 27% of clouds between −5°C and −10°C contained a supercooled layer, falling to 10% of clouds between −15°C and −20°C and 6% between −25°C and −30°C. Below −30°C the frequency of occurrence falls suddenly, and below −40°C, where liquid water droplets are known to freeze spontaneously, a supercooled layer was diagnosed erroneously only once, and then only for 4.5 minutes.

Because the detection of one liquid water layer by our algorithm precludes the detection of another in the same profile, the results have been expressed as the fraction of clouds *in a given 5°C temperature interval* that contain a layer, rather than the fraction of all clouds. Of course, one would expect the fraction of clouds containing a layer in a 10°C interval to be proportionately greater than that for the 5°C

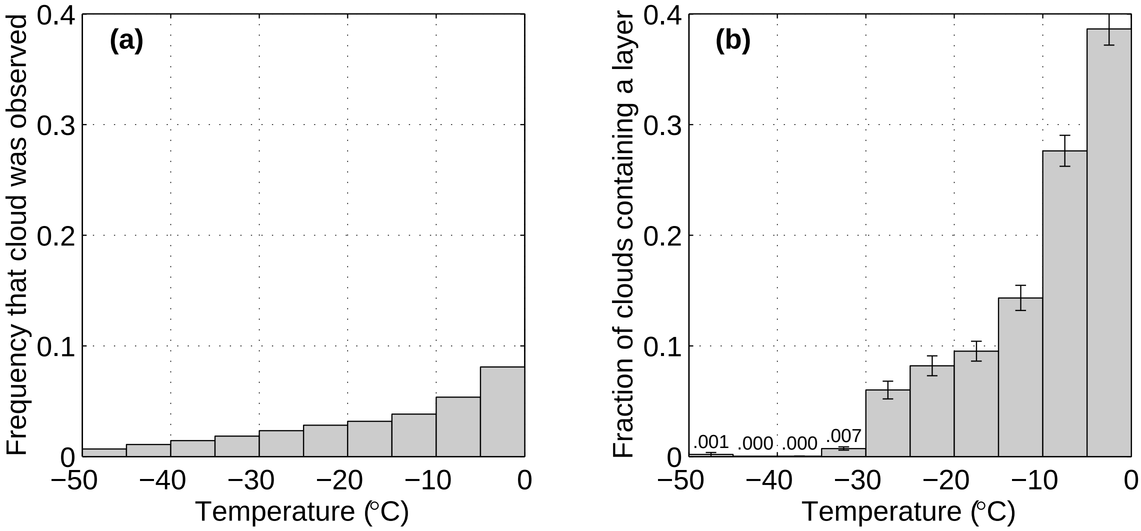

Figure 4.4: Statistics of the occurrence of highly reflective layers attributable to liquid water in the data taken by the Chilbolton lidar ceilometer in 2000 when it was operating at 5° from zenith: (a) the fraction of observations in which cloud was seen in each 5°C temperature interval (less than the true cloud occurrence due to extinction by intervening cloud); (b) the fraction of these clouds that contained a highly reflective layer.

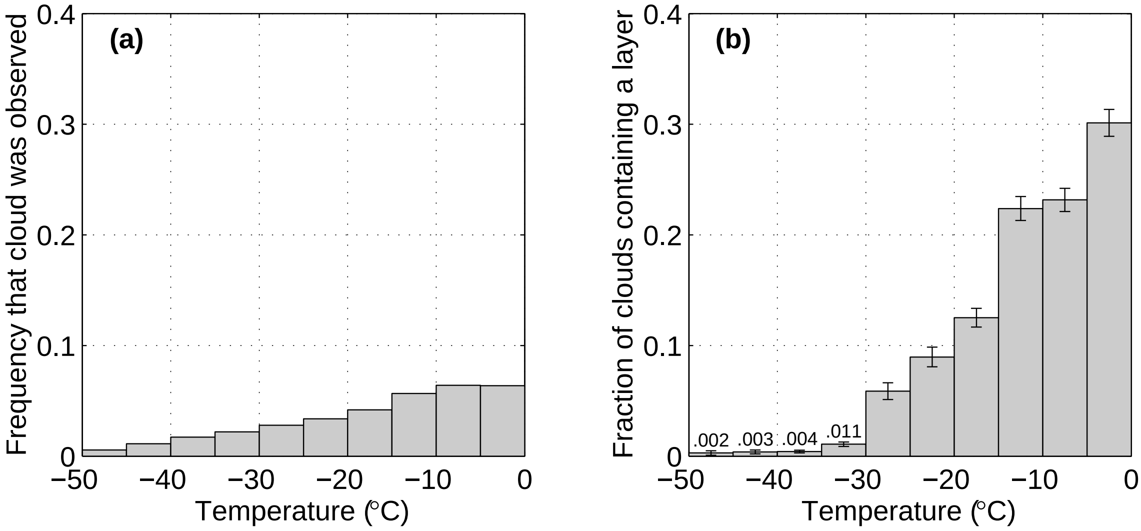

Figure 4.5: Statistics of the occurrence of highly reflective layers in data taken by the Cabauw lidar operating at 5° from zenith.

interval. It should also be noted that the representation in Figs. 4.4b and 4.5b is not equivalent to the ratio of liquid water content to total condensate that has been presented by authors such as Moss and Johnson (1994); due to the much smaller particle size, liquid water tends to be more radiatively effective than ice for the same water content, and our results are categorized by optical depth rather than water content.

Figure 4.5 shows similar statistics obtained by the lidar at Cabauw, also operating at 5° from zenith. The data were taken between October 2001 and July 2002, and the length of the dataset was equivalent to 287 days of continuous observation. Temperature profiles were extracted from the daily ECMWF model forecasts over the site. Panel a shows that the amount of cloud detected was not significantly different from Chilbolton. The frequency of occurrence of supercooled layers (shown in panel b) exhibits a similar similar decrease with decreasing temperature as observed at Chilbolton, but with a greater frequency between -20 and -10°C, and a lower frequency between -10 and 0°C. Of course, the climates of Chilbolton and Cabauw are very similar, and considerably more lidar data would need to be analysed to establish with confidence the extent to which supercooled cloud occurrence varies with geographical location; a spaceborne lidar would be particularly suited to this purpose.

At this point we should question the representativity of these results even for the sites at which they were obtained, since no supercooled clouds can be detected by ground-based lidar in the presence of obscuring low-level liquid water cloud. This immediately excludes important types of mixed-phase cloud from the statistics, most notably precipitating fronts. However, it should be pointed out that other techniques can also be susceptible to uneven sampling. For example, passive remote sensing from space only measures the phase of cloud top, while aircraft datasets (such as that analysed by Moss and Johnson 1994) can inevitably contain a large but unrepresentative number of ‘interesting’ frontal systems at the exclusion of ‘less interesting’ clouds such as altocumulus, due to the fact that the decision on which clouds to sample is subjective. Therefore we regard the statistics here as complementary to those obtained by other studies.

4.4.2 Specular reflection from horizontally aligned plate crystals

To demonstrate the problems that can be experienced by the algorithm when it is applied to data taken by lidar pointing directly at zenith, Fig. 4.6 shows a 12-h section of β' (panel a) and γ_w (panel b) in an altocumulus cloud observed at zenith. Until around 05:30 UTC, the strongest echo was from the -15°C liquid layer at cloud top, where γ_w approached the asymptote corresponding to an infinite optical depth, as in Figs. 4.1 and 4.2. From 05:30 to 07:30, however, the strongest backscatter was intermittently to be found 500-1000 m below the liquid water layer, and here γ_w exceeded the theoretical asymptotic value by more than a factor of 3. This indicates that the enhanced backscattered echo was not accompanied by any significant increase in extinction, i.e. that k had a very low value. The same phenomenon was observed by Platt (1977), who attributed it to specular reflection from horizontally aligned plate crystals. It therefore does not indicate any significant enhancement of the radiative importance of the ice, and is not observed in data taken away from zenith. It is our experience that this phenomenon tends to occur most often beneath liquid water layers, which is consistent with the observations in Hogan *et al.* (2003b) of high differential reflectivity beneath supercooled liquid layers, indicating the presence of horizontally aligned, high-density pristine crystals.

Figure 4.7 shows the statistics for cloud detection and supercooled water occurrence obtained for the Chilbolton lidar between 22 April and 30 November 1999, when it was pointing at zenith. Again, temperature was obtained from the Met Office model. Comparing Fig. 4.7b to Fig. 4.4b in can be seen that the effect of specular reflection is to increase the fraction of clouds containing a layer by 0.05-0.1 between -20°C and -10°C, which is precisely the region where one would expect plate crystals to exist. At other temperatures the occurrence is generally very similar. The phenomenon of specular reflection is examined in much more detail elsewhere in this report.

4.4.3 Horizontal extent of supercooled water layers

Figure 4.8a shows the mean layer duration as a function of mean layer temperature, for the three datasets presented in Figs. 4.4, 4.5 and 4.7. The value plotted is actually the ‘expected value’ of the duration of a layer, *given that a layer has been detected.* This way the mean is weighted towards the long-lived clouds

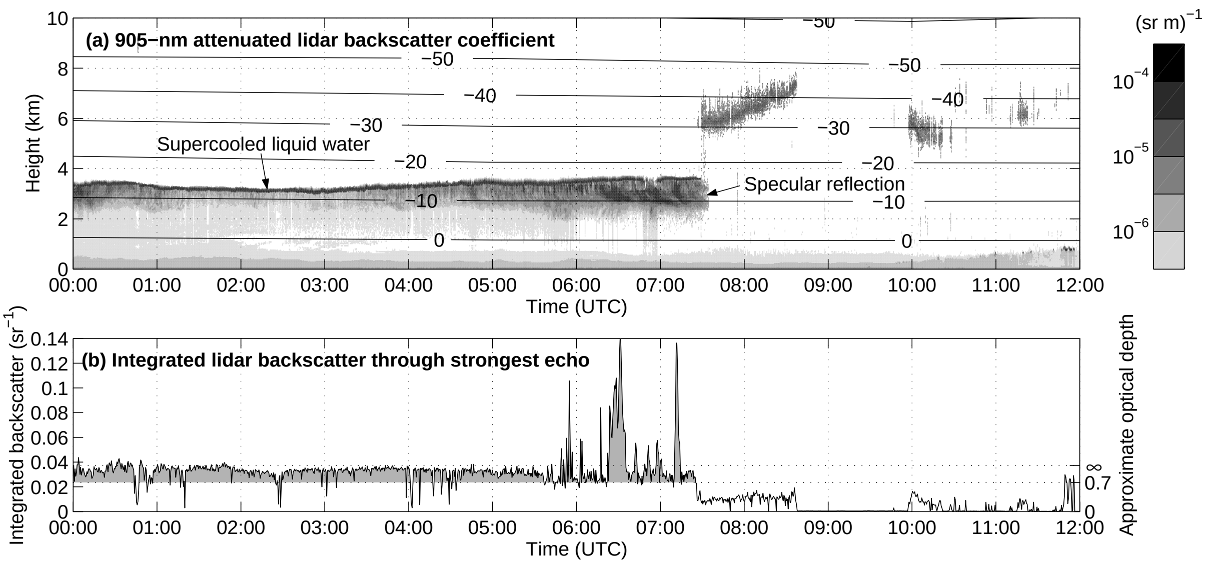

Figure 4.6: Example of specular reflection observed by zenith-pointing lidar at Chilbolton on 17 October 2002. As in Figs. 4.1 and 4.2, panel b depicts the integrated backscatter in a 300 m vertical window encompassing the strongest echo. The temperature contours were obtained by interpolating in time between four radiosonde ascents from Larkhill, 25 km to the west of Chilbolton.

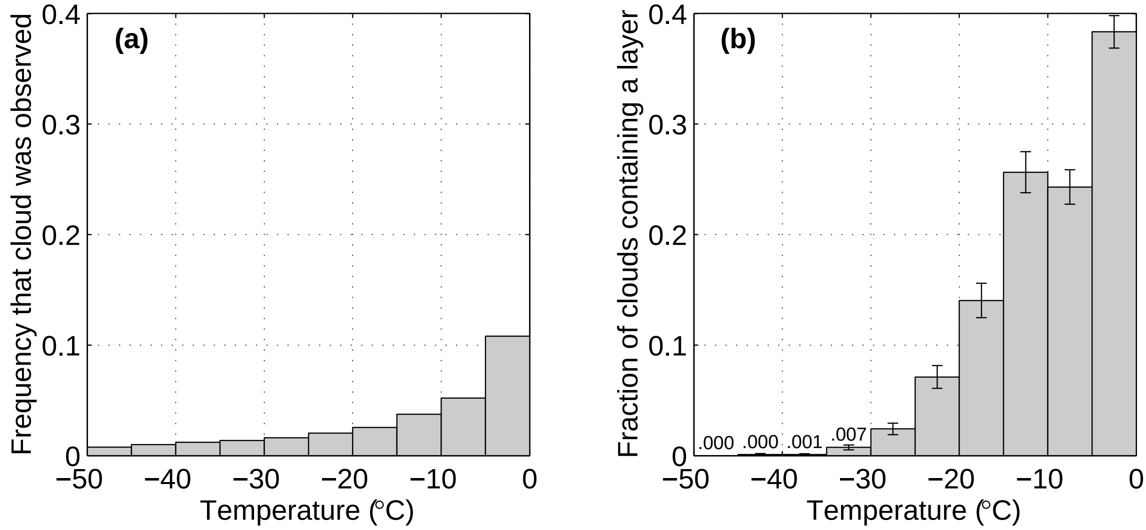

Figure 4.7: Statistics of the occurrence of highly reflective layers in data taken by the Chilbolton lidar in 1999 when it was operating at zenith.

that contribute most to the total fraction of clouds containing a supercooled layer, rather than being weighted towards the numerous small clouds that persist for only a few minutes but do not contribute significantly to the total. Because of the frequent temporary obscuration of the layers by passing low level cumulus, layers were deemed continuous in this analysis if any gaps in them lasted no longer than 10 minutes, although it is recognised that the resulting layer durations may still be underestimated because of the possibility of obscuration for periods longer than 10 mins.

Horizontal extent was calculated from layer duration using the wind speed over the site, from the Met Office model in the case of Chilbolton, and from the ECMWF model in the case of Cabauw. It can be seen that the mean horizontal extent of layers warmer than $-30°$C observed at 5° from zenith typically

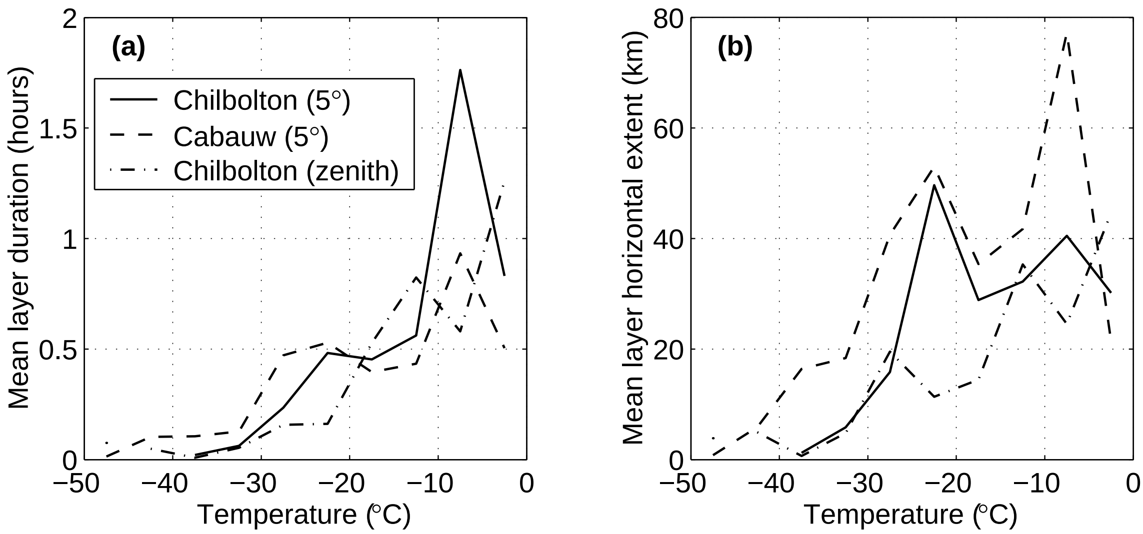

Figure 4.8: Mean duration and horizontal extent of individual layers versus temperature, for the three datasets shown in Figs. 4.4, 4.5 and 4.7.

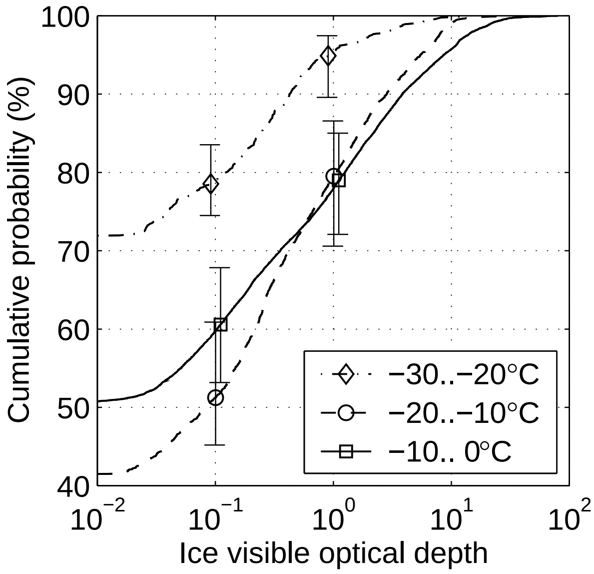

Figure 4.9: Cumulative probability distribution of the optical depth of the ice cloud above layers of supercooled water in three different temperature ranges. The observations used were from Chilbolton in 2000, when the lidar was operated at 5° from zenith to avoid specular reflection from aligned crystals.

varied between 20 and 70 km, with a tendency for more extensive layers over Cabauw than Chilbolton. The layers observed at zenith appear to have been somewhat less horizontally extensive on average. At temperatures below -30°C, the few layers that were detected by the algorithm typically persisted for less than 6 mins.

4.4.4 Optical depth of cirrus above supercooled water layers

We next use radar reflectivity to estimate the optical depth distribution of the ice cloud overlaying the supercooled liquid water clouds. Chilbolton data are analysed from 2000 when the lidar operated in an off-zenith configuration, in order to be confident that almost all the highly reflective layers observed were composed of liquid water. The *Galileo* radar was available until 17 October 2000, and the lidar was available for the whole year except 12 January to 26 April, leaving 147 days in which radar, lidar and model data were available. Layers were diagnosed from the lidar β' profile as before, and the optical depth of any cirrus above them was found by integrating the extinction coefficient derived from Z up from the height of the layer to the highest radar echo.

The results are shown in Fig. 4.9, divided according to the temperature of the supercooled cloud. It is found that around 20% of supercooled clouds between 0°C and −20°C had ice cloud above with an optical depth in excess of 1, falling to 5% of supercooled clouds between −20°C and −30°C. These values increase when ice optical depths of greater than 0.1 are considered, lying between 20% and 50% depending on the temperature. The error bars of up to ±10% indicate the range of uncertainty associated with the use of radar reflectivity to estimate ice optical depth. The same analysis was performed on the 196 days of 1999 for which radar, lidar and model data were available, and the results were very similar.

The radiative transfer calculations performed in the previous chapter suggested that in cloud profiles containing both liquid water and ice, the supercooled liquid water would have a stronger net effect on the radiation budget than the ice for ice optical depths of up to around 1, in the daytime. By considering only the longwave flux reported in the previous chapter, we estimate that at night the supercooled water has a stronger effect only when any ice above has an optical depth of less than approximately 0.1. Therefore the results presented here indicate that, when present, supercooled liquid water will dominate the radiative properties of a cloud profile in over 80% of daytime cases, and in more than half of nighttime cases.

The relatively low sensitivity of the radar in the last few months of the dataset mean that some radiatively significant ice cloud may not have been detected, particularly in the upper troposphere. Therefore the fraction of supercooled clouds that dominate the radiative properties of the cloud profile may be overestimated. Conversely, there will be occasions when the lidar sees only the lowest of several liquid water layers embedded within an ice cloud, in which case the relative importance of the ice will be overestimated. A particular example of this is the mixed-phase cloud observed by airborne lidar on 20 October 1998 in the previous chapter, which contained four individual liquid water layers. The coldest layer occurred at the top of the mid-level cloud, yet for the ground-based lidar it was completely obscured by the lowest of the layers 2 km below.

4.4.5 Comparison of observed occurrence of supercooled water with values in the ECMWF and UK Met Office models

In this section we compare the observed occurrence of supercooled water at Chilbolton by lidar pointing 5° from zenith (Fig. 4.4b) with the occurrence in a year of data from both the ECMWF model and the mesoscale version of the Met Office Unified Model over Chilbolton. The model data are taken from April 1999 to March 2000 inclusive. The models are rather different in the way they represent cloud; the Met Office model carries separate prognostic variables for ice content and liquid/vapour content, the division between liquid and vapour being diagnosed mainly from temperature (Smith 1990), while the ECMWF model has separate prognostic variables for vapour and condensed water, with the ice/liquid water ratio being diagnosed purely as a function of temperature (Matveev 1984).

We apply the same 0.7 optical-depth threshold in the model as in the observations. The effective radius of liquid water clouds over land is 10 μm in the ECMWF model (J.-J. Morcrette, personal communication), so a model layer is deemed to contain a layer if the liquid water path of the cloudy part of the gridbox (calculated using the model cloud fraction) exceeds 4.7 g m^{-2}. The Met Office used a

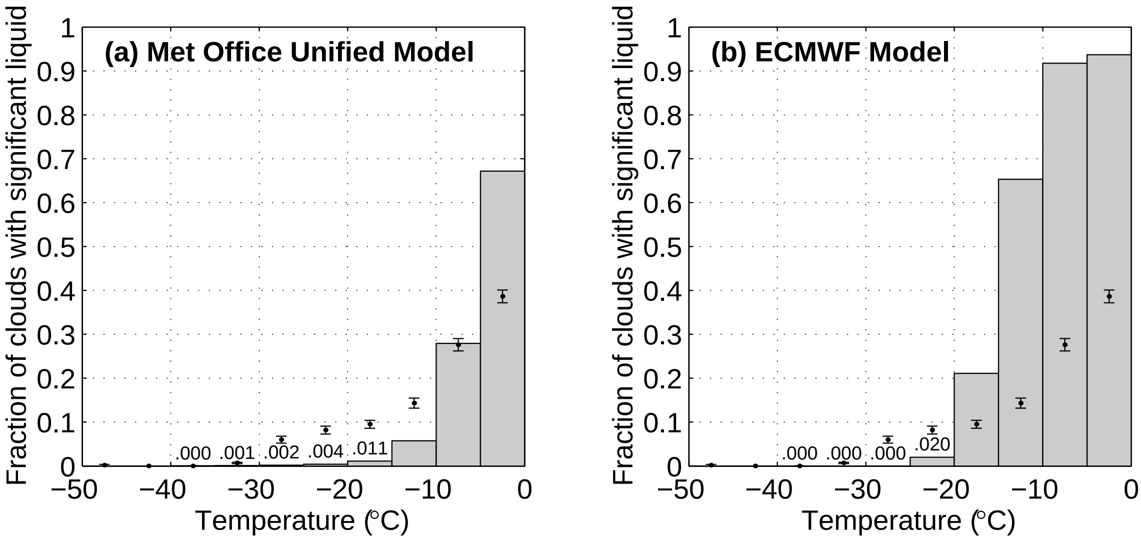

Figure 4.10: The grey bars depict the frequency of supercooled water clouds over Chilbolton in (a) the mesoscale version of the UK Met Office model and (b) the ECMWF model. The superimposed error bars show the observed values, taken from Fig. 4.4b.

constant value of 7 μm over land until 12 October 1999, after which they moved to a parameterization in which the number concentration of droplets was kept constant and the size was allowed to change (J. M. Edwards, personal communication). For consistent analysis of the Met Office model data, we assume a constant value of 7 μm for the whole period, which equates to a critical liquid water path of 3.3 g m^{-2}. Gridboxes with a cloud fraction of less than 0.05 are rejected from the analysis.

Figure 4.10 shows the fraction of model clouds in each 5°C temperature interval that contain significant liquid water, with the observations from Fig. 4.4b depicted by the superimposed error bars. The comparison clearly indicates that supercooled liquid water in the models tends to occur too frequently at warmer temperatures and too infrequently at colder temperatures, although the occurrence was considerably more in the ECMWF model than in the Met Office model. Neither model contained significant liquid water at temperatures below -20°C, although in the case of the ECMWF model, the diagnostic ice/liquid ratio does not allow liquid to exist at temperatures below -23°C.

The clouds in the Met Office model were also found to contain supercooled liquid water around 25% more frequently in the winter than the summer (not shown). This could be because stratocumulus, which is common throughout the year, is more likely to be supercooled in winter, although no similar trend was evident in the lidar observations. The ECMWF model with its diagnosed liquid/ice fraction exhibited no seasonal dependence.

A number of factors could contribute to the difference between the observations and the models. In the case of the models, the 500-750 m vertical resolution in the mid-troposphere would certainly make it difficult to simulate supercooled clouds anything like those observed with lidar, which are typically only 150 m thick. Also, the model does not represent the sub-gridscale fluctuations in vertical velocity that are likely to be responsible for the condensation of liquid water. On the other hand, the representativity of the observations is questionable because they exclude the majority of fronts due to obscuration by low-level cloud, yet the mixed-phase cloud scheme in the Met Office model was formulated principally with fronts in mind.

4.5 Conclusions

The frequency of occurrence of stratiform supercooled liquid water clouds as a function of temperature has been characterized by utilizing the fact that liquid water tends to be strikingly visible in lidar imagery as highly reflective layers apparently around 150 m thick. An algorithm has been developed that utilizes the integrated backscatter to identify occurrences of supercooled liquid water with an optical depth greater than 0.7. Between $-5°$C and $-10°$C, around 27% of clouds at Chilbolton were found to contain a supercooled liquid water layer, the probability falling steadily with temperature to essentially zero below $-35°$C. Operating at zenith was found to bias the statistics between $-20°$C and $-10°$C, due to specular reflection from horizontally aligned plate crystals at this temperature. It should be noted that these results may not be representative of all types of mixed-phase clouds since obscuration by low cloud means that they unavoidably exclude precipitating frontal systems and deep convection. They are also restricted to one particular climatic zone.

Concurrent radar observations suggested that less than half of the layers had ice above them with an optical depth of more than 0.1, and less than 20% had ice above with an optical depth greater than 1. Given the significant optical depths of the layers themselves, and considering the radiative transfer calculations performed in the previous chapter, this demonstrates that in the majority of cases where supercooled water is present it dominates the radiative properties of the cloud profile, and therefore is likely to be important for climate.

Many forecast and climate models still parameterize mixed-phase clouds using a simple ratio between liquid and ice water content which varies with temperature alone, but lidar observations show mixed-phase clouds to be far from homogeneously mixed. Altocumulus was commonly observed in the ground-based lidar data used in this chapter, and consists of a thin liquid water layer beneath which ice is falling; this scenario of liquid over ice cannot be simulated by such models. Fig. 4.10 indicates that the temperature dependence of the fraction of clouds containing radiatively significant liquid water is considerably in error. Before these findings can be used to improve models one must determine the underlying causes of the phenomenon that could be used as a basis for parameterization, and whether any of the more sophisticated microphysical parameterizations already in existence have any skill. A first step would be to compare individual instances of supercooled cloud with model parameters such as vertical velocity, stability, humidity and Richardson Number. However, we would not expect good representation of thin liquid layers in models until vertical resolutions in the mid-troposphere are improved. Work to simulate these clouds in a cloud-resolving model is currently in progress.

Satellite measurements of supercooled clouds have been reported from the POLDER (Polarization and Directionality of the Earth Reflectances) instrument on board the ADEOS platform. Goloub *et al.* (2000) measured the polarization properties of reflected sunlight at up to 14 different angles, and identified the occurrence of liquid water droplets by the presence of a sharp peak in the polarized radiance near the 'rainbow' angle of 140°. Analysis of 120×10^6 km^2 of coincident ATSR-2 infrared data obtained on a single day by Giraud *et al.* (2001) suggested that the probability of a cloud being composed of ice was a quasi-linear function of cloud top temperature, falling from nearly 100% at around $-33°$C to close to 0% at $-10°$C. Conversely, Riedi *et al.* (2001) compared the POLDER retrieval with the cloud top temperature derived using radar and lidar on the 201 days that the instrument flew over the Atmospheric Radiation Measurement (ARM) site in Oklahoma, and found a sharp transition from purely liquid to purely ice at $-33°$C.

Comparison of these ground-based results with the POLDER satellite measurements discussed in the introduction reveals some agreements but raises questions. The lidar/radar studies suggest a steady decrease in the occurrence of liquid water with temperature as reported by Giraud *et al.* (2001), rather than the step change at $-33°C$ inferred by Riedi *et al.* (2001). However, Giraud *et al.* (2001) suggest that the large brightness temperature differences observed between 11 and 12 μm, previously ascribed to semi-transparent cirrus (Inoue 1985) are in fact indicative of semi-transparent liquid water clouds, arising because the refractive index of liquid water cloud is also higher at 12 μm than 11 μm. The lidar data presented here do not support this hypothesis as the layers detected are by no means semi-transparent; indeed, the principal criterion for their identification is that they have a high backscatter coefficient, which implies that they are optically thicker than any ice cloud of the same physical thickness is likely to be. This ties in with the suggestion of Heymsfield *et al.* (1991) that supercooled altostratus are physically similar to stratocumulus, since stratocumulus certainly tend not to be semi-transparent. It would therefore be very interesting to compare ground-based lidar observations directly with cloud phase inferred from POLDER or other passive spaceborne instruments, such as MODIS (the Moderate Resolution Imaging Spectroradiometer; see Strabala *et al.* 1994 and Baum *et al.* 2000).

References

Baum, B. A., Soulen, P. F., Strabala, K. L., King, M. D., Ackerman, S. A., Menzel, W. P., and Yang, P., 2000: Remote sensing of cloud properties using MODIS airborne simulator imagery during SUCCESS. 2. Cloud thermodynamic phase. *J. Geophys. Res.*, **105,** 11781–11792.

Brown, P. R. A., and Francis, P. N., 1995: Improved measurements of the ice water content in cirrus using a total-water probe. *J. Atmos. Oceanic Tech.,* **12,** 410–414.

Brown, P. R. A., Illingworth, A. J., Heymsfield, A. J., McFarquhar, G. M., Browning, K. A., and Gosset, M., 1995: The role of spaceborne millimeter-wave radar in the global monitoring of ice-cloud. *J. Appl. Meteorol.,* **34,** 2346–2366.

Eloranta, E. W., 1998: A practical model for the calculation of multiply scattered lidar returns. *Appl. Opt.,* **37,** 2464–2472.

Francis, P. N., Hignett, P., and Macke, A., 1998: The retrieval of cirrus cloud properties from aircraft multi-spectral reflectance measurements during EUCREX'93. *Q. J. R. Meteorol. Soc.,* **124,** 1273–1291.

Gibson, A. J., Thomas, L., and Bhattacharyya, S. K., 1977: Some characteristics of cirrus clouds deduced from laser radar observations at different elevation angles. *J. Atmos. Terr. Phys.,* **29.,** 657–660.

Giraud, V., Thouron, O., Riedi, J., and Goloub, P., 2001: Analysis of direct comparison of cloud top temperature and infrared split window signature against independent retrievals of cloud thermodynamic phase. *Geophys. Res. Lett.,* **28,** 983–986.

Goloub, P., Herman, M., Chepfer, H., Riedi, J., Brogniez, G., Couvert, P. and Seze, G., 2000: Cloud thermodynamical phase classification from the POLDER spaceborne instrument. *J. Geophys. Res. Atmos.,* **105,** 14747–14759.

Heymsfield, A. J., Miloshevich, L. M., Slingo, A., Sassen, K., and Starr, D. O'C., 1991: An observational and theoretical study of highly supercooled altocumulus. *J. Atmos. Sci.,* **48,** 923–945.

Hogan, R. J., and Illingworth, A. J., 1999: The potential of spaceborne dual-wavelength radar to make global measurements of cirrus clouds. *J. Atmos. Oceanic Tech.,* **16,** 518–531.

Hogan, R. J., Jakob, C., and Illingworth, A. J., 2001: Comparison of ECMWF cloud fraction with radar-derived values. *J. Atmos. Oceanic Technol.* **40,** 513–525.

Hogan, R. J., Bouniol, D., Ladd, D. N., O'Connor, E. J. and Illingworth, A. J., 2003a: Absolute calibration of 94/95-radars using rain. *J. Atmos. Oceanic Technol.,* **20,** 572–580.

Hogan, R. J., Francis, P. N., Flentje, H., Illingworth, A. J., Quante, M., and Pelon, J., 2003b: Characteristics of mixed-phase clouds - 1. Lidar, radar and aircraft observations from CLARE'98. *Q. J. R. Meteorol. Soc.,* **129,** 2089–2116.

Hogan, R. J., Illingworth, A. J., E. J. O'Connor and J. P. V. Poiares Baptista, 2003c: Characteristics of mixed-phase clouds - 2. A climatology from ground-based lidar. *Q. J. R. Meteorol. Soc.,* **129,** 2117–2134.

Illingworth, A. J., R. J. Hogan, A. C. A. P. van Lammeren, D. P. Donovan, F. H. Berger, T. Halecker, C.-L. Liu, A. Feijt and H. I. Bloemink, 2000: Quantification of the synergy aspects of the Earth Radiation Mission, Final report, ESTEC Contract 13167/98/NL/GD.

Inoue, T., 1985: On the temperature and effective emissivity determination of semi-transparent cirrus clouds by bi-spectral measurements in the 10 micron window region. *J. Meteorol. Soc. Japan,* **63,** 88–99.

Liebe, H. J., 1985: An updated model for millimeter-wave propagation in moist air. *Radio Sci.,* **20,** 1069–1089.

Matveev, L. T., 1984: *Cloud Dynamics.* D. Reidel, 340 pp.

McFarquhar, G. M., and Heymsfield, A. J., 1997: Parameterization of tropical cirrus ice crystal size distributions and implications for radiative transfer: Results from CEPEX. *J. Atmos. Sci.,* **54,** 2187–2200.

Moss, S. J., and Johnson, D. W., 1994: Aircraft measurements to validate and improve numerical model parametrizations of ice to water ratios in clouds. *Atmos. Res.,* **34,** 1–25.

O'Connor, E. J., Illingworth, A. J., and Hogan, R. J., 2003: A technique for auto-calibration of cloud lidar. *Submitted to J. Atmos. Oceanic Technol.*

Pinnick, R. G., Jennings, S. G., Chylek, P., Ham, C., and Grandy, W. T., 1983: Backscatter and extinction in water clouds. *J. Geophys. Res.,* **88,** 6787–6796.

Platt, C. M. R., 1973: Lidar and radiometric observations of cirrus clouds. *J. Atmos. Sci.,* **30,** 1191–1204.

Platt, C. M. R., 1977: Lidar observation of a mixed-phase altostratus cloud. *J. Appl. Meteorol.,* **16,** 339–345.

Platt, C. M. R., Abshire, N. L., and McNice, G. T., 1978: Some microphysical properties of an ice cloud from lidar observation of horizontally oriented crystals. *J. Appl. Meteorol.,* **17,** 1220–1224.

Riedi, J., Goloub, P., and Marchand, R. T., 2001: Comparison of POLDER cloud phase retrievals to active remote sensor measurements at the ARM SGP site. *Geophys. Res. Lett.* **28,** 2185–2188.

Sassen, K., 1984: Deep orographic cloud structure and composition derived from comprehensive remote sensing measurements. *J. Climate Appl. Meteorol.,* **23,** 568–583.

Sassen, K., 1991: The polarization lidar technique for cloud research—a review and current assessment. *Bull. Am. Met. Soc.,* **72,** 1848–1866

Smith, R. N. B., 1990: A scheme for predicting layer clouds and their water content in a general circulation model. *Q. J. R. Meteorol. Soc.,* **116,** 435–460.

Strabala, K. I., Ackerman, S. A., and Menzel, W. P., 1994: Cloud properties inferred from 8-12-μm data. *J. Appl. Met.,* **33,** 212–229.

Thomas, L., Cartwright, J. C., and Wareing, D. P., 1990: Lidar observations of the horizontal orientation of ice crystals in cirrus clouds. *Tellus,* **42B,** 211–216.

Chapter 5

Estimate of the global distribution of stratiform supercooled liquid water clouds using the LITE lidar

Summary. In this chapter, data from the Lidar In-space Technology Experiment (LITE), which flew on the space shuttle in 1994, are used to estimate the fraction of clouds colder than 0°C that contain supercooled liquid water, utilizing the fact that they may be easily distinguished from ice by their high backscatter coefficient and sharp backscatter gradient at cloud top. Although only 10.5 hours of data were used, this corresponds to a total distance of 2.8×10^5 km and therefore represents a reasonable global snapshot. Around 20% of clouds between -10°C and -15°C were found to contain liquid water, falling with temperature to essentially zero below -35°C. Even from this limited dataset some clear latitudinal clear trends were evident, with a distinctly more frequent occurrence of supercooled water in clouds associated with mid-latitude weather systems in the southern hemisphere, as well as in tropical clouds warmer than around -15°C. The results between 40 and 60°N agree well with the distribution previously found at Chilbolton in Southern England (51°N), implying that the forthcoming long-term lidar observations from space will be able to infer the global distribution of mixed-phase clouds with much greater accuracy and vertical resolution than has been possible until now.

5.1 Introduction

For measurements of the type shown in the previous chapter to be of maximum use for models they really need to be made around the whole globe. The potential of spaceborne cloud lidar was demonstrated by the LITE instrument, which operated for 53 hours over a latitude range of $\pm60°$ from the space shuttle *Discovery* in September 1994 (Winker et al. 1996). It has been used to evaluate the clouds in the model of the European Centre for Medium-range Weather Forecasts (Miller et al. 1999), although only for a very limited snapshot. As supercooled water tends to occur at the top of cold clouds (Rauber and Tokay 1991), there is an advantage in viewing the scene from above as there is much less obscuration by intervening cloud. In this chapter we use LITE data to show how the global distribution of stratiform supercooled liquid water clouds can be estimated from spaceborne lidar. Although the sampling period was very short, the coverage was sufficient to build up reasonable statistics as a function of latitude and temperature, and thereby demonstrate what will be possible from long-term satellite lidar missions, such as IceSat launched in January 2003 (Zwally et al. 2002), Calipso, due for launch in spring 2005 (Winker et al. 2002), and EarthCARE.

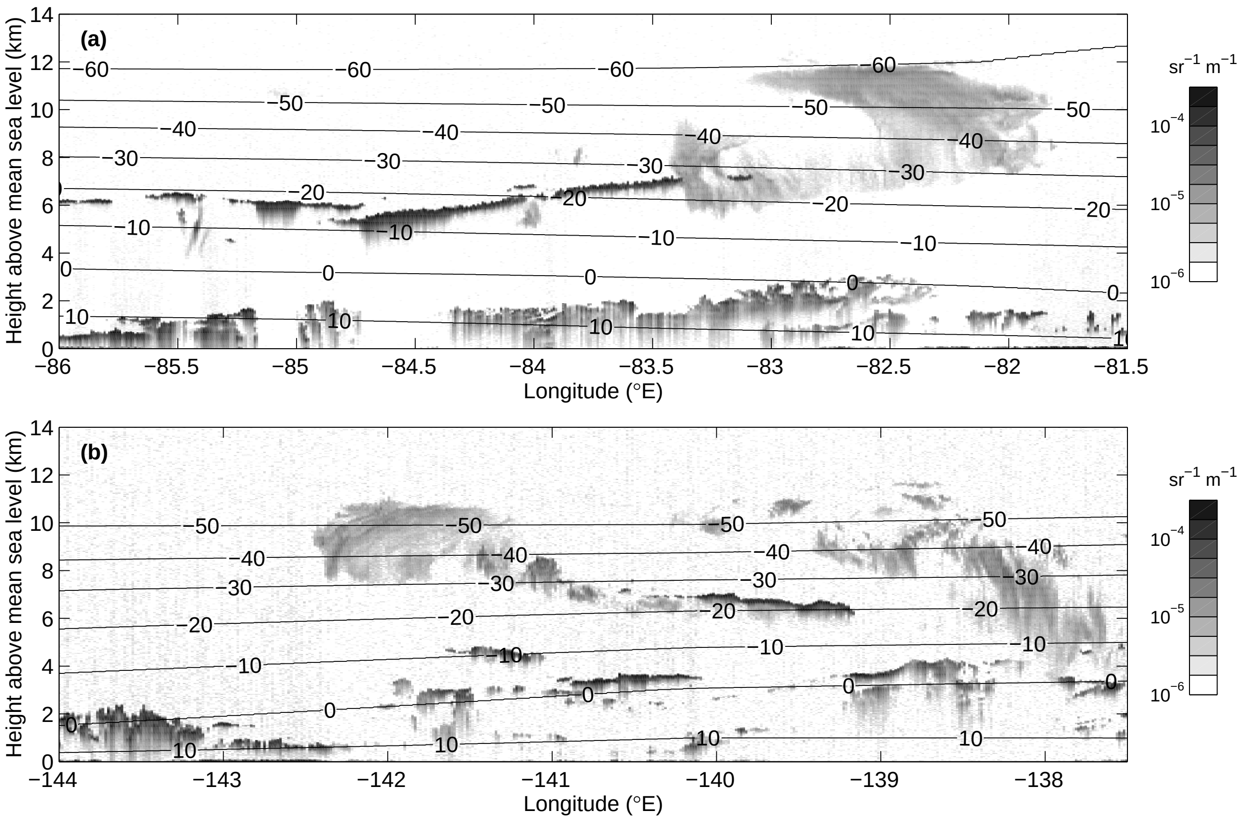

Figure 5.1: Backscatter coefficient at 532 nm from LITE during two 90-s periods containing supercooled liquid water layers, with temperature from the NCEP analysis superimposed: (a) from orbit 72 on 14 September 1994, between the latitudes of -31.5°N and -36.2°N; (b) from orbit 135 on 18 September 1994, between latitudes of 49.6°N and 46.4°N.

5.2 Method

Figure 5.1 shows two examples of LITE data in which both ice and supercooled liquid water clouds were observed. There is a distinct difference in appearance between the purely ice clouds (such as those centered at -82.5°E in Fig. 5.1a and at -142°E and -138°E in Fig. 5.1b) and the thin but highly reflective layers which are believed to be composed of liquid water. This difference in the backscatter profiles provides a basis by which an algorithm may distinguish between the two.

The analysis method is similar to that used in the previous chapter. Lidar profiles are examined in turn, and in each 5°C temperature interval we determine both whether a cloud was observed and whether a liquid layer was identified. The fraction of clouds containing significant liquid water in each 5°C temperature interval is then simply the number of liquid water observations divided by the number of observations of a cloud of any phase. In thick clouds the lidar signal can be completely extinguished, which causes the total cloud fraction to be underestimated, but since neither a cloud nor a liquid water layer are identified below the region of full extinction, the statistics are unaffected. The temperature was taken from the analyses of the National Centers for Environmental Prediction, provided as part of the standard LITE product. It should be noted that we are concerned primarily with stratiform clouds; supercooled water in the cores of cumulonimbus clouds is much less radiatively important due to the much lower areal coverage and the fact that convective cores would still be very optically thick even if supercooled water were not present.

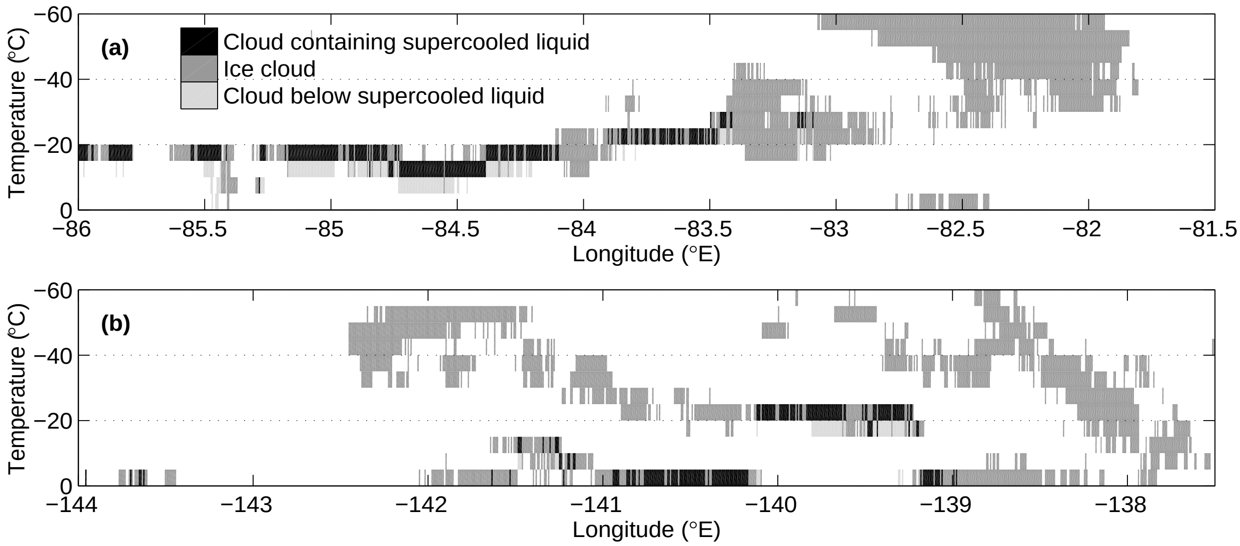

Figure 5.2: Diagnosis of purely ice cloud and cloud containing supercooled water in each 5°C temperature interval, for the two cases shown in Fig. 5.1. The light gray areas are clouds detected by the lidar but rejected from the analysis because they lie beneath a higher supercooled liquid layer and the algorithm is unable to confidently determine their phase.

Wavelengths of 1064 nm, 532 nm and 355 nm were available, but the 532-nm channel was used as it was found to have the best cloud detection. The data were available with 15 m vertical resolution and 700-m along-track averaging. Cloud was distinguished from instrument noise by using the top 32 pixels (480 m) of each profile to characterize the noise; cloudy pixels were deemed to be those that had a backscatter more than four standard deviations above the median noise level. To reduce the probability of contamination by speckle noise, each 5°C temperature interval was deemed to contain cloud only if 4 or more pixels (not necessarily adjacent) within it lay above the threshold. To minimize contamination by aerosols, data in the lowest 2 km above the surface were not used, although as the 0°C isotherm was usually above this height, the effect on the statistics was small.

The algorithm described in the previous chapter involved integrating the backscatter coefficient through the 300 m around the highest backscatter value in a profile. Utilizing the fact that the extinction-to-backscatter ratio of liquid cloud droplets is approximately constant, the algorithm could thereby be formulated to only identify liquid water layers with an optical depth greater than 0.7. However, this approach requires that the lidar return does not saturate the receiver. Unfortunately, due to the limited dynamic range of the LITE instrument, when the receiver gain was set high enough for reasonable detection of optically thin ice clouds, the reflective nature of liquid water layers meant that they tended to cause receiver saturation.

We therefore use a much simpler algorithm: a liquid water layer is diagnosed if the maximum attenuated lidar backscatter coefficient in the profile exceeds a trigger level of 2.5×10^{-4} sr^{-1} m^{-1} and the backscatter falls by more than a factor of 20 in the 200 m above the peak value. Profiles are analysed only if the gain setting permits attenuated backscatter measurements of at least 3×10^{-4} sr^{-1} m^{-1} without saturation, thus providing a 20% "headroom" above the trigger level. In fact, only 10.5 hours of LITE data satisfied this criterion, although it should be pointed out that this corresponds to a total distance of 2.8×10^{5} km, which is equivalent to nearly 6 months of observations from a ground-based lidar assuming a mean cloud-level wind speed of 20 m s^{-1}. This gain setting meant that aerosols were generally not detected which helped to minimize the chance of them biasing the estimate of cloud occurrence.

This algorithm permits only one liquid layer to be detected in each profile, which is not a significant limitation as the first layer in a profile containing several layers generally attenuates the signal such that the lower layers are not detected. Nonetheless, cloud echos detected below a liquid water layer are removed from the cloud occurrence statistics as even if they were composed of liquid water, they could not contribute to the liquid layer statistics. It should be noted that the highest layer in a profile is usually the one that influences the radiative fluxes the most (shown in an earlier chapter); any lower layers are less important.

The values of the parameters used in the algorithm are justified by the agreement with liquid water layers identified subjectively from LITE imagery, and later by the agreement with ground-based lidar using a more sophisticated algorithm based on integrated backscatter. Nonetheless, it is appreciated that more robust results should be possible from future lidars such as IceSat, for which the 1064 nm channel uses a lower gain receiver in order not to saturate, while the 532 nm channel uses a higher gain and so is more sensitive to clouds.

Figure 5.2 demonstrates the diagnosis of supercooled water versus temperature for the two cases shown in Fig. 5.1. Note that no attempt is made to diagnose layers lower than 2 km above the surface. The algorithm shows considerable skill in identifying the reflective layers in, although it should be noted that some layers are missed because extinction by ice clouds higher in the profile reduces the backscatter of the layer to an extent that it does not trigger the algorithm. This will result in a slight underestimate of the frequency of occurrence of supercooled water.

5.3 Results

Figure 5.3 depicts the frequency that cloud of any phase was observed by LITE as a function of latitude, height and temperature. Although this will be an underestimate of the true cloud fraction due to the effects of lidar extinction, the cloud associated with tropical anvil cirrus and mid-latitude weather systems is clearly apparent, as well as the depleted cloud amount beneath the descending branch of the southern hemisphere Hadley Cell.

The fraction of these clouds that contained a supercooled liquid water in each 5°C temperature interval is shown in Fig. 5.4. A clear tendency for the occurrence of supercooled water to decrease with falling temperature is observed, with no significant liquid water detected below around -35°C. The existence of enhanced supercooled water between 10°S and 30°N at temperatures down to -10°C could be explained by the previously reported occurrence of shallow convective clouds in the tropics that tend to reach a level of neutral buoyancy a short way above the melting level (Johnson et al. 1999), and possibly detrain into layers at that level. The abundance of supercooled water between 30°S and 60°S at temperatures down to -30°C is presumably associated with the southern hemisphere storm track, although it is intriguing that so much more supercooled water is observed than at the same latitude band in the northern hemisphere. We await much longer data series from the forthcoming spaceborne lidar missions to further explore the latitudinal and seasonal differences and seek explanations for them.

Lastly we compare spaceborne observations of cloud and supercooled water occurrence with values obtained from the ground. Figure 5.5 shows the LITE lidar retrievals between 40°N and 60°N together with the same parameters estimated from one year of lidar data at Chilbolton in southern England (51°N). The Chilbolton data were reported in the previous chapter, and calculated using a more sophisticated algorithm that utilized the integrated backscatter. Figure 5.5a demonstrates the much better sampling of cold clouds from space; from the ground higher clouds are frequently obscured by the pres-

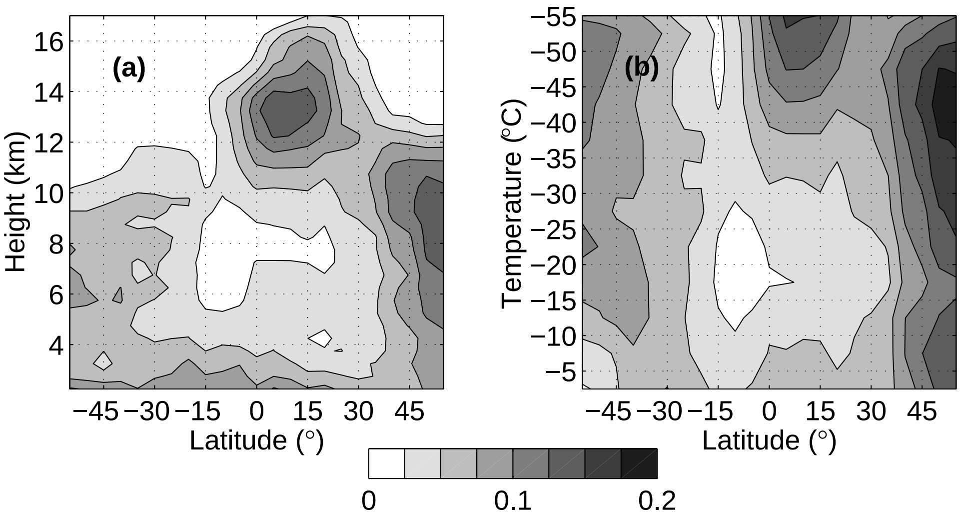

Figure 5.3: Fraction of pixels in which cloud was observed versus (a) height and latitude; (b) temperature and latitude.

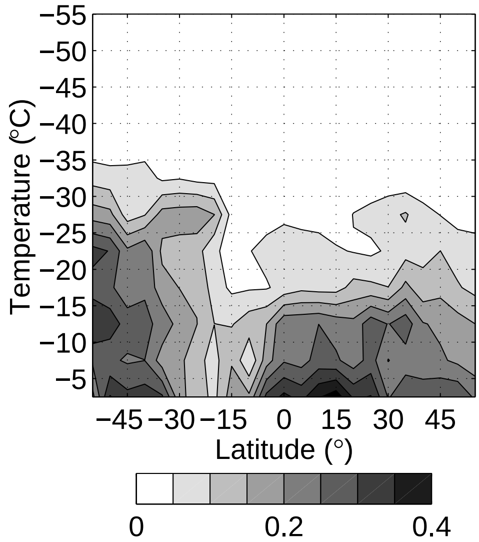

Figure 5.4: Fraction of clouds in each 5°C temperature interval containing a supercooled liquid layer.

ence of optically thick boundary-layer clouds. The results from space are also much closer to the mean cloud fraction values in the range 0.15–0.2 found by Hogan et al. (2001) for heights between 2 and 9 km using ground-based cloud radar at Chilbolton.

Figure 5.5b shows good agreement between the occurrence of supercooled water from space and the ground, particularly at temperatures colder than -10°C. This is encouraging as one might have expected a single site to be atypical and ground-based lidar observations to be somewhat biased as they exclude the mixed-phase regions of frontal systems due to extinction by low-level cloud. The layers evident in Fig. 5.1 have a horizontal extent of the order of 100 km. Unfortunately it was not possible to do a more systematic study of the distribution of supercooled cloud lengths because of the frequent interruption of the retrievals by changes in the receiver gain setting.

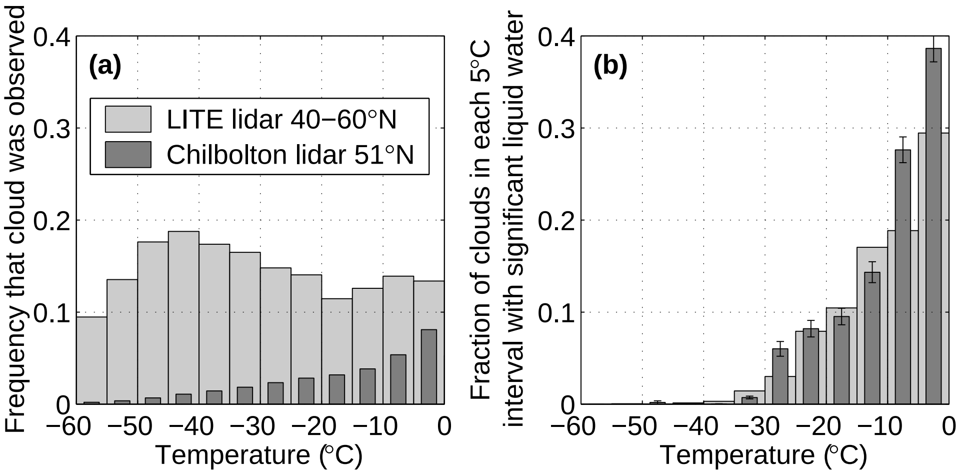

Figure 5.5: Comparison of lidar observations from LITE between 40°N and 60°N and from Chilbolton at 51°N: (a) fraction of pixels above 2 km observed to be cloudy; (b) fraction of clouds in each 5°C temperature interval containing a supercooled layer.

5.4 Conclusion

We have shown that spaceborne lidar has the potential to provide very valuable information on the distribution of stratiform supercooled liquid water clouds around the globe, which could play an important role in the global radiation balance. Despite the limitations of the LITE instrument, the statistics produced agree very well with those obtained by ground-based lidar, and give us confidence that the tendencies exhibited in Fig. 5.4 are robust.

A much more complete study will soon be possible with data from long-term satellite missions IceSat, Calipso and EarthCARE. IceSat is in a high polar orbit (latitude range ±86°), allowing statistics on the phase of polar clouds to be studied. The long term coverage will also allow more subtle aspects of supercooled clouds to be characterized, such as their dependence on orographic forcing and cloud type. It will also be possible to evaluate the representation of mixed-phase clouds in forecast and climate models. Calipso and EarthCARE will have depolarization capability, allowing cloud phase to be determined with much greater confidence. The availability of coincident or near-coincident spaceborne cloud radar in both cases will enable the observations of supercooled clouds to be put in the context of the full cloud profile.

References

Hogan, R. J., C. Jakob and A. J. Illingworth, Comparison of ECMWF winter-season cloud fraction with radar derived values, *J. Appl. Meteorol.,* **40,** 513–525, 2001.

Johnson, R. H., T. M. Rickenbach, S. A. Rutledge, P. E. Ciesielski and W. H. Schubert, Trimodal characteristics of tropical convection, *J. Climate*, **12,** 2397–2418, 1999.

Miller, S. D., G. L. Stephens and A. C. M. Beljaars, A validation survey of the ECMWF prognostic cloud scheme using LITE, *Geophys. Res. Lett.,* **26,** 1417–1420, 1999.

Rauber, R. M, and A. Tokay, An explanation for the existence of supercooled water at the top of cold clouds, *J. Atmos. Sci.,* **48,** 1005–1023, 1991.

Winker, D. M., R. H. Couch, and M. P. McCormick, An overview of LITE: NASA's Lidar In-space Technology Experiment, *Proc. IEEE,* **84,** 164–180, 1996.

Winker, D. M., J. Pelon and M. P. McCormick, The CALIPSO Mission: Aerosol and Cloud Observations from Space, *ILRC 21 (Lidar Remote Sensing in Atmospheric and Earth Sciences),* Quebec City, Quebec, 8-12 July 2002.

Zwally, H. J., B. Schutz, W. W. Abdalati, J. Abshire, C. Bentley, A. Brenner, J. Bufton, J. Dezio, D. Hancock, D. Harding, T. Herring, B. Minster, K. Quinn, S. Palm, J. Spinhirne and R. Thomas, ICESat's laser measurements of polar ice, atmosphere, ocean, and land, *J. Geodynamics,* **34,** 405–445, 2002.